BMAL1 drives muscle repair through control of hypoxic NAD$^+$ regeneration in satellite cells

Pei Zhu,[1,2] Noah X. Hamlish,[1,2] Abhishek Vijay Thakkar,[1,2] Adam W.T. Steffeck,[1,2] Emily J. Rendleman,[1,3] Nabiha H. Khan,[1,3] Nathan J. Waldeck,[2] Andrew W. DeVilbiss,[4] Misty S. Martin-Sandoval,[4] Thomas P. Mathews,[4] Navdeep S. Chandel,[1,5] and Clara B. Peek[1,2]

[1]Department of Biochemistry and Molecular Genetics, Northwestern University Feinberg School of Medicine, Chicago, Illinois 60611, USA; [2]Department of Medicine, Division of Endocrinology, Metabolism, and Molecular Medicine, Northwestern University Feinberg School of Medicine, Chicago, Illinois 60611, USA; [3]Simpson Querrey Institute for Epigenetics, Northwestern University Feinberg School of Medicine, Chicago, Illinois 60611, USA; [4]Children's Research Institute, Department of Pediatrics, University of Texas Southwestern Medical Center, Dallas, Texas 75235, USA; [5]Department of Medicine, Division of Pulmonary and Critical Care, Northwestern University Feinberg School of Medicine, Chicago, Illinois 60611, USA

The process of tissue regeneration occurs in a developmentally timed manner, yet the role of circadian timing is not understood. Here, we identify a role for the adult muscle stem cell (MuSC)-autonomous clock in the control of muscle regeneration following acute ischemic injury. We observed greater muscle repair capacity following injury during the active/wake period as compared with the inactive/rest period in mice, and loss of *Bmal1* within MuSCs leads to impaired muscle regeneration. We demonstrate that *Bmal1* loss in MuSCs leads to reduced activated MuSC number at day 3 postinjury, indicating a failure to properly expand the myogenic precursor pool. In cultured primary myoblasts, we observed that loss of *Bmal1* impairs cell proliferation in hypoxia (a condition that occurs in the first 1–3 d following tissue injury in vivo), as well as subsequent myofiber differentiation. Loss of *Bmal1* in both cultured myoblasts and in vivo activated MuSCs leads to reduced glycolysis and premature activation of prodifferentiation gene transcription and epigenetic remodeling. Finally, hypoxic cell proliferation and myofiber formation in *Bmal1*-deficient myoblasts are restored by increasing cytosolic NAD$^+$. Together, we identify the MuSC clock as a pivotal regulator of oxygen-dependent myoblast cell fate and muscle repair through the control of the NAD$^+$-driven response to injury.

[*Keywords*: NAD$^+$; circadian rhythm; hypoxia; muscle regeneration; muscle stem cell]

Supplemental material is available for this article.

Received September 28, 2021; revised version accepted January 5, 2022.

Disrupted circadian function is strongly associated with metabolic pathologies, including diabetes, obesity, cancer, skeletal muscle myopathy, and accelerated aging (Bass and Takahashi 2010; Bass and Lazar 2016). However, gaps remain in our understanding of how clocks interact with developmental stage-specific timing mechanisms to maintain healthy metabolic control and healthy tissue maintenance across the life span. The mammalian "core" clock consists of a transcription–translation feedback loop in which bHLH-PAS transcriptional activators CLOCK and BMAL1 orchestrate circadian phase-specific induction of gene expression, including genes encoding their own repressors, PER1–3, and CRY1–2. PERs and CRYs are regulated post-translationally via phosphorylation, degradation, and intracellular trafficking. Following their translocation to the nucleus, PERs and CRYs negatively regulate the CLOCK/BMAL1 heterodimeric activator complex. An additional "core" clock loop involves the regulation of *Bmal1* synthesis by the competitive actions of the nuclear hormone receptors REV-ERBα/β and RORα/β (Takahashi 2015).

Cell-autonomous molecular clocks direct the timing of cell type-specific functions as well as anticipate tissue-specific environmental stressors. For example, the molecular clock in mature skeletal muscle controls the rhythmic expression of metabolic proteins to adapt to the daily changes in muscle metabolic demand imposed from feeding and movement (McCarthy et al. 2007;

Corresponding author: c-peek@northwestern.edu
Article published online ahead of print. Article and publication date are online at http://www.genesdev.org/cgi/doi/10.1101/gad.349066.121.

© 2022 Zhu et al. This article is distributed exclusively by Cold Spring Harbor Laboratory Press for the first six months after the full-issue publication date (see http://genesdev.cshlp.org/site/misc/terms.xhtml). After six months, it is available under a Creative Commons License (Attribution-NonCommercial 4.0 International), as described at http://creativecommons.org/licenses/by-nc/4.0/.

Dyar et al. 2014; Harfmann et al. 2016). Furthermore, we and others have previously demonstrated that the mature skeletal muscle clock can direct the activity of the hypoxia-inducible factor (HIF) pathway, a major regulator of metabolic and hypoxic stress that occurs in muscle during strenuous exercise and ischemic injury (Peek et al. 2017; Vaughan et al. 2020). However, little is known about the role of clock HIF regulation during muscle regeneration, a process that also requires hypoxia signaling through the HIF pathway (Majmundar et al. 2015; Beaudry et al. 2016; Yang et al. 2017). Specifically, exposure to hypoxia controls the maintenance and activation of muscle stem cells (MuSCs, also called satellite cells), a small nonmyofiber cell population responsible for muscle growth and repair (Beaudry et al. 2016). It has also been proposed that MuSCs undergo extensive metabolic reprogramming toward anaerobic glycolysis to adapt to localized hypoxic stress associated with muscle injury. This "hypoxic window" following injury is essential for the expansion of myoblast progenitor populations prior to differentiation into myofibers (Ly et al. 2020; Relaix et al. 2021). Thus, metabolic control by environmental cues (e.g., hypoxia) is a central component of MuSC-mediated muscle regeneration, and we therefore hypothesized that clock-regulated hypoxia adaptation is central to this process. Importantly, several studies have indicated a link between circadian clock factors and the proliferation of MuSCs (Chatterjee et al. 2013, 2015; Katoku-Kikyo et al. 2021).

In this study, we demonstrate that time of day dictates skeletal muscle repair capacity following injury in vivo, with more rapid regeneration occurring after injury during the night, which is the active phase for mice. Using conditional genetics, we show that the autonomous clock within activated MuSCs and myoblasts is essential for muscle repair, proper myogenesis, and adaptation to hypoxia. Finally, our findings indicate a role for the molecular clock in MuSC metabolic adaptation to hypoxic environments following muscle tissue injury through the regulation of anaerobic glycolysis and cytosolic NAD^+ regeneration.

Results

Muscle repair following tissue injury is time of day-dependent and requires the autonomous muscle stem cell clock

To assess the impact of the circadian clock and time of day on muscle repair, we used a frequently used model for injury of mouse skeletal muscle in which cardiotoxin (CTX) is injected into the tibialis anterior (TA) muscle of the hindleg (Couteaux et al. 1988; Chargé and Rudnicki 2004; Bentzinger et al. 2013; Hardy et al. 2016). Damage incurred by CTX injection is rapid, resulting in disruption of myofiber arrangement, variation in myofiber size, and widening of the interstitial space between myofibers at the site of delivery within 1 h (Mahdy et al. 2016). Therefore, we reasoned that administration of this injurious toxin in the morning versus the evening would reveal phase-specific differences in the regenerative response. We delivered CTX during the early rest period for the mouse (zeitgeiber time [ZT] 4) as well as the early active period (ZT16) and assessed muscle repair by histology 7 d following injury (Supplemental Fig. S1A). We observed less repair of the damaged muscle tissue following injury at ZT4 versus ZT16 by histological quantification of muscle fiber size and size distribution at the site of injury, consistent with a recent study (Supplemental Fig. S1; Katoku-Kikyo et al. 2021). To test whether time of day control of muscle regeneration is affected by feeding and/or activity differences at the time of tissue collection, we repeated the experiment in which mice were collected at a phase opposite to the time of injury (6.5 dpi) (Fig. 1A). We observed a difference in muscle fiber repair between mice injured at ZT16 and ZT4 similar to that observed at 7 dpi, indicating that the time of muscle injury influences the extent of repair, with greater repair following injury during the active phase (ZT16) (Fig. 1B–D). The time of day difference in muscle regeneration prompted us to ask whether muscle repair is under the control of the circadian clock. Indeed, consistent with an earlier report (Chatterjee et al. 2013), we observed significantly impaired muscle repair following CTX injury in mice lacking the core clock activator *Bmal1* throughout the body (Supplemental Fig. S2). However, this does not elucidate the contributions of peripheral cell clocks versus central nervous system (CNS) clocks such as those that control rhythmic behavioral feeding and activity. Since the regenerative capacity of skeletal muscle in response to injury relies on a rare population of adult MuSCs residing between the basal lamina and sarcolemma of muscle fibers (Yin et al. 2013), we hypothesized that MuSC clocks might underlie time of day differences in regeneration. To determine the contribution of the adult MuSC-autonomous circadian clock to muscle regeneration, we generated adult life-inducible muscle stem cell-specific *Bmal1* (*Bmal1*^{musc}) knockout mice (*Pax7-CreER; Bmalfx*$^{/fx}$) (Murphy et al. 2011). Using an additional lineage-tracing allele (fx-STOP-fx-tdTomato), we were able to confirm ~82.3% loss of *Bmal1* within *Pax7*$^+$ cells after intraperitoneal tamoxifen delivery (Supplemental Fig. S3A–D). Following CTX-mediated muscle injury at ZT16, the time of day corresponding to the peak of *Bmal1* expression in MuSCs (Solanas et al. 2017), *Bmal1*^{musc} mice displayed reduced muscle fiber regeneration at both 7 and 14 d postinjury (Fig 1E). This is apparent by quantification of fiber size distribution at the site of injury (Fig. 1F,G) as well as mean muscle fiber size (Fig. 1H), demonstrating a requirement for the adult MuSC molecular clock in muscle tissue injury repair.

Our observation of greater muscle repair following injury at ZT16 versus ZT4 in wild-type mice prompted to us to ask how this relates to levels of *Bmal1* expression. In mature mouse skeletal muscle tissue, as well as other peripheral tissues such as the liver, peak *Bmal1* gene expression occurs in the early rest period (approximately ZT0–4) in mice (McCarthy et al. 2007; Koike et al. 2012; Dyar et al. 2014). Notably, peak of *Bmal1* expression in quiescent MuSCs is higher at ZT16 than at ZT4 (Supplemental Fig. S3E), aligning with the time at which we observed more efficient muscle regeneration (Fig. 1B–D). However, further experimentation will be required to determine

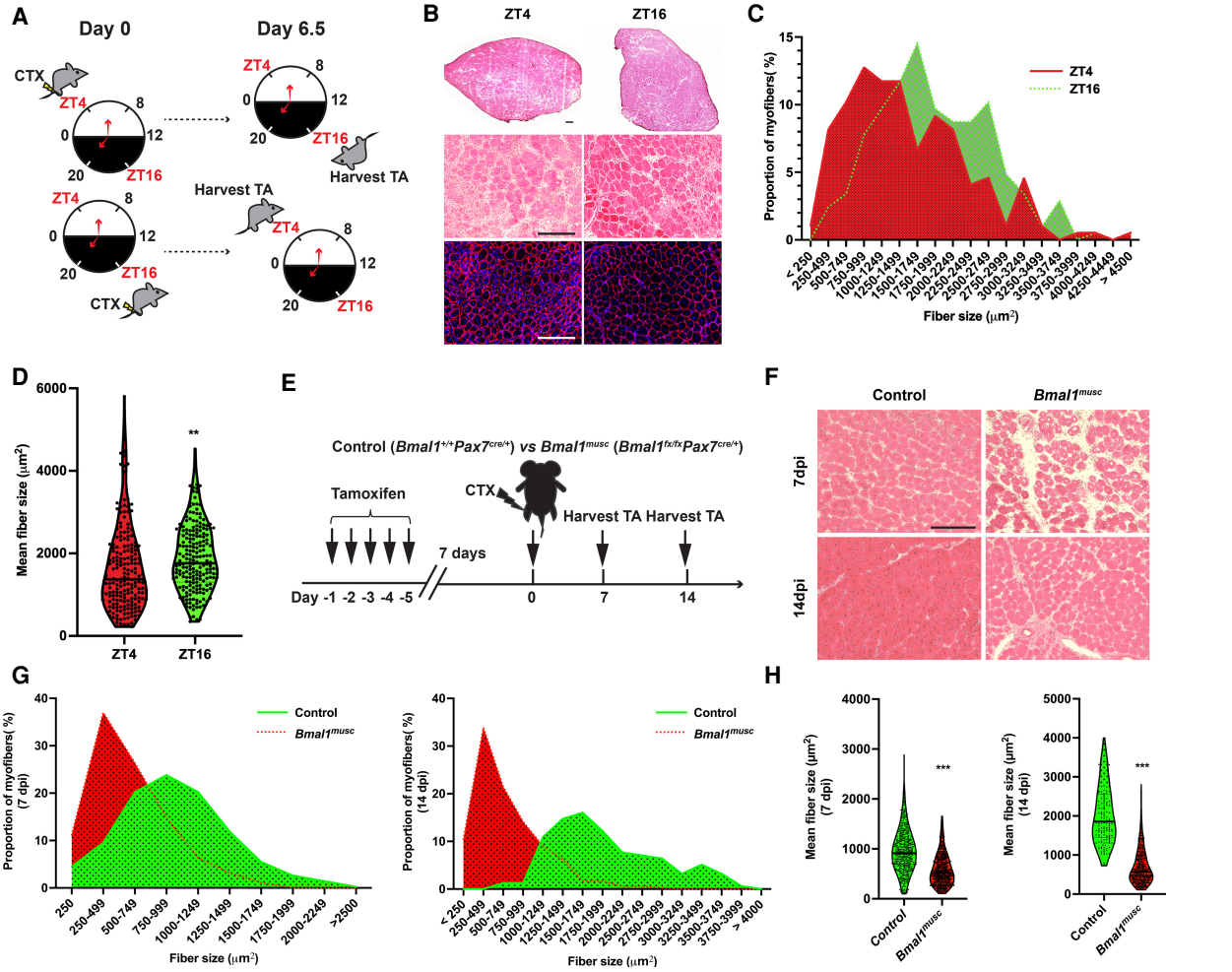

Figure 1. Muscle regeneration following injury depends on time of day and the muscle stem cell-autonomous circadian clock. (*A*) Experimental design: WT mice were injured with cardiotoxin (CTX) injection into TA muscles at ZT4 or ZT16. Muscles were harvested at the opposite time point at 6.5 d postinjury (dpi). $n = 5$ mice per group. (*B*) Representative H&E- and laminin-stained sections of regenerating TA muscles at the site of injury. Scale bar, 200 µm. (*C*,*D*) Muscle fiber size (cross-sectional area [CSA]) distribution (*C*) and quantification of the mean CSA (*D*) of nascent myofibers of regenerating TA muscles from WT mice injured at ZT4 and ZT16. (**) $P < 0.01$ by two-sided unpaired Student's *t*-test. (*E*) Experimental design: Adult control and *Bmal1*^{musc} mice received five consecutive daily intraperitoneal injections of 100 mg/kg tamoxifen in corn oil. After 7 d, mice were injected with CTX in TA muscles and examined for muscle regeneration at 7 and 14 dpi. $n = 6$ mice per group. (*F*) Representative H&E-stained sections of regenerating TA muscles from control and *Bmal1*^{musc} mice at 7 and 14 dpi. Scale bar, 200 µm. (*G*,*H*) Fiber size (CSA) distribution (*G*) and quantification of the CSA (*H*) of nascent myofibers of regenerating TA muscles from control and *Bmal1*^{musc} mice at 7 and 14 dpi. Data are represented as mean ± SEM. (***) $P < 0.001$ by two-sided unpaired Student's *t*-test.

whether maximal repair aligns with the peak of BMAL1 transcriptional activity.

BMAL1 regulates primary myoblast proliferation and differentiation

It has been shown in diverse animal models that muscle injury coincides with a sharp decrease in oxygen concentrations around the damaged site within the first hours to days (Józsa et al. 1980; Kang et al. 2013; Scheerer et al. 2013; Hardy et al. 2016)—a time at which the activated MuSCs begin propagating to give rise to sufficient myonuclei before differentiation (Scicchitano et al. 2016; Forcina et al. 2020). Indeed, we observed induction of the hypoxia-responsive factor HIF1α in TA muscles on days 1 and 3 after CTX injury (Supplemental Fig. S4A). In addition, analysis of previously published transcriptomic data from MuSCs isolated at different time points following CTX injury (Latroche et al. 2017) revealed that the expression of HIF1α and its canonical target genes, including *Vegfa*, *Cxcr4*, and *Epo*, increase sharply after injury, peak at 2 dpi, and return to baseline by 4 dpi (Supplemental Fig. S4B), suggesting that MuSCs are under hypoxic stress during the early stages of muscle regeneration. Our prior studies have established a role of the circadian clock in the regulation of glycolytic and oxidative metabolism and in

the control of the HIF response to hypoxia, leading us to hypothesize that hypoxic response to injury may be subjected to circadian control (Peek et al. 2017). To investigate the role of the circadian clock transcription pathway specifically within proliferating myoblasts, we first measured the impact of *Bmal1* loss on the proliferative response of primary myoblasts obtained from TA muscle tissues of wild-type and *Bmal1*$^{-/-}$ C57b6/J mice when maintained either under normoxia (21% O_2) or hypoxia (1% O_2) for 24 h. We observed a major reduction in cell number by cell counting with loss of *Bmal1*, which was exaggerated in hypoxia (Fig. 2A), suggesting a role for *Bmal1* in the

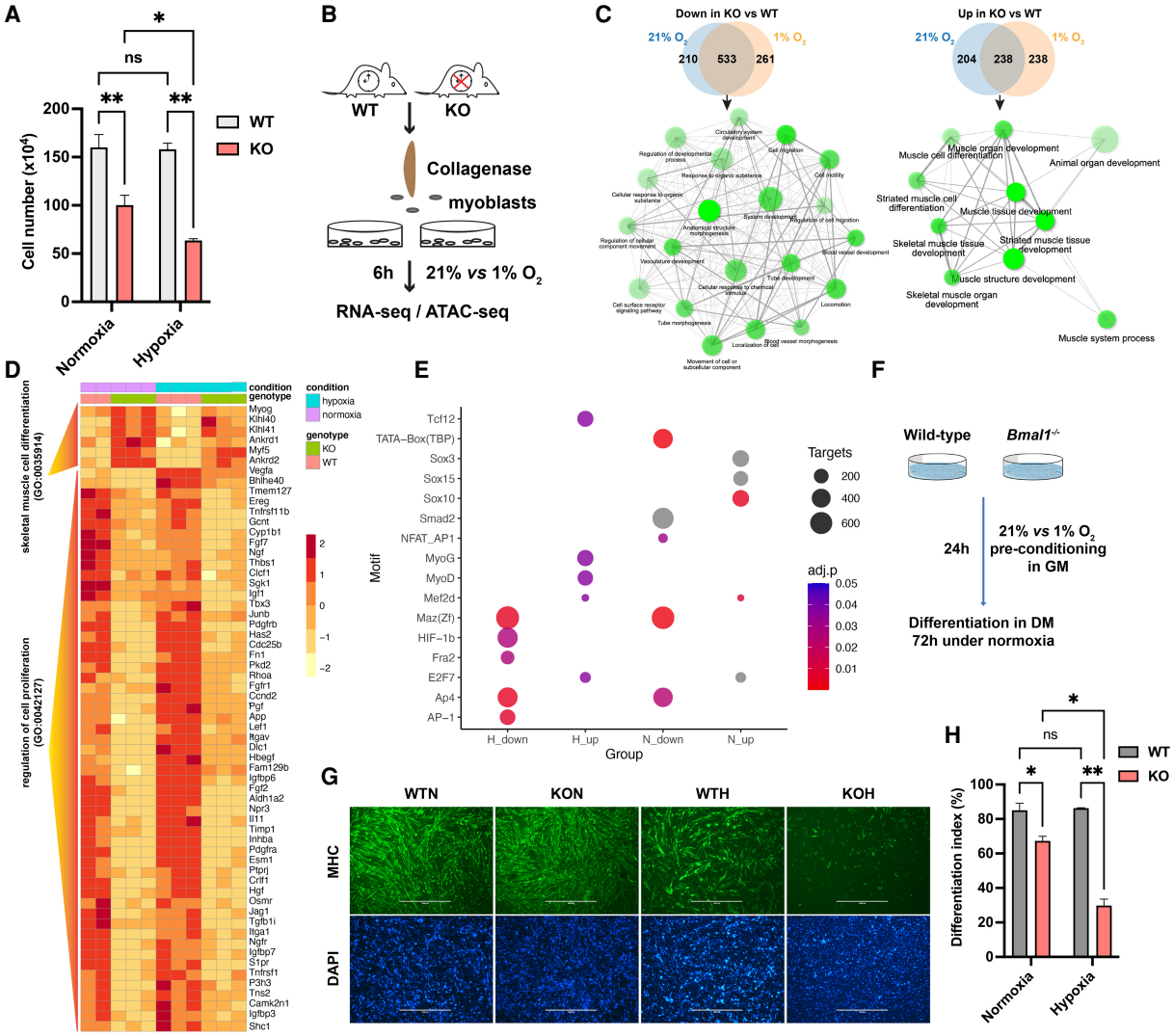

Figure 2. The myoblast circadian clock controls cell proliferation and differentiation in hypoxia. (*A*) Cell number quantification by hemocytometer of WT and *Bmal1*$^{-/-}$ (KO) primary mouse myoblasts following exposure to normoxia (N; 21% O_2) or hypoxia (H; 1% O_2) for 24 h. (*) $P < 0.05$, (**) $P < 0.01$ by two-way ANOVA with Tukey's multiple comparisons test. (n.s.) Nonsignificant. (*B*) Experimental design: RNA and ATAC sequencing of WT and *Bmal1*$^{-/-}$ myoblasts following 6 h in normoxia or hypoxia. $n = 3$ per condition. (*C*) Gene ontology analysis using ShinyGO to determine pathway enrichment of differentially expressed genes (DEGs) between WT and *Bmal1*$^{-/-}$ myoblasts in normoxia and hypoxia. A subset of genes with detectable expression (average normalized counts >0) from the myoblast RNA-seq data set (19,862 genes in total) was used as the background gene set. (*D*) Heat map of DEGs important for cell proliferation and cell differentiation that are enriched in WT and *Bmal1*$^{-/-}$ myoblasts, respectively. (*E*) MRF DNA motif enrichment within promoters of the DEGs between *Bmal1*$^{-/-}$ and WT myoblasts. A subset of genes with detectable expression (average normalized counts >0) from the myoblast RNA-seq data set (19,862 genes in total) was used as the background gene set. Dot sizes are proportional to the number of target sequences containing the indicated motif. Dot colors are proportional to adjusted *P*-value. (H) Hypoxia, (N) normoxia. (*F*) Experimental design: measurement of myogenic capacity in WT and *Bmal1*$^{-/-}$ myoblasts following 24 h of preconditioning in normoxia versus hypoxia. (*G*,*H*) Myosin heavy chain (MHC, *top*) and DAPI (*bottom*) staining (*G*) and quantification of differentiation index presented as the percentage of MHC$^+$ nuclei (*H*) following 72 h in differentiation medium. Scale bar, 1000 µm. Data are represented as mean ± SEM. (*) $P < 0.05$, (**) $P < 0.01$ by two-way ANOVA with Tukey's multiple comparisons test. (n.s.) Nonsignificant.

adaptation to hypoxic environments. To investigate whether impaired cell proliferation of *Bmal1*$^{-/-}$ myoblasts might be due to differences in BMAL1-regulated transcription, we performed RNA sequencing of WT and *Bmal1*$^{-/-}$ myoblasts following exposure to normoxia or hypoxia for 6 h (Fig. 2B; Supplemental Fig. S5A). We observed significantly up-regulated (443 in normoxia vs. 477 in hypoxia) and down-regulated (745 in normoxia vs. 796 in hypoxia) genes in *Bmal1*$^{-/-}$ cells compared with wild type, with a large degree of overlap between hypoxia and normoxia, although the fold change of differential gene expression was generally greater under hypoxia versus normoxia (Supplemental Fig. S5B,C). Gene ontology analysis of significantly up-regulated or down-regulated genes in *Bmal1*$^{-/-}$ myoblasts (in both oxygen conditions) revealed enrichment of cell proliferation and muscle differentiation pathways (Fig. 2C; Supplemental Fig. S5D). Specifically, *Bmal1*$^{-/-}$ myoblasts displayed reduced expression of positive regulators of cell proliferation and increased expression of promyogenic (i.e., myofiber differentiation) genes (Fig 2D). Consistent with this, the master regulator of differentiation, MYOG, was increased at the protein level in *Bmal1*$^{-/-}$ myoblasts—an effect that was enhanced in hypoxia (Supplemental Fig. S5E). We also observed increased enrichment of DNA motifs for myogenic regulatory factors (MRFs) within promoter regions of genes more highly expressed in *Bmal1*$^{-/-}$ cells versus wild type in hypoxia, including *MyoG* and *MyoD* (Fig. 2E). This enrichment was not observed in genes more highly expressed in wild-type versus *Bmal1*$^{-/-}$ myoblasts, indicating a specific increase in MRF activity with loss of *Bmal1*. Collectively, our cell proliferation and RNA sequencing data (Fig. 2A–C) point toward reduced cell proliferation and premature differentiation of *Bmal1*$^{-/-}$ myoblasts during a time when myoblasts are normally dividing and differentiation is suppressed.

To assess the phenotypic impact of *Bmal1* disruption on myoblast differentiation, we cultured wild-type and *Bmal1*$^{-/-}$ cells in prodifferentiation medium and measured the formation of multinucleated myofibers as well as the presence of myosin heavy chain (MHC), a mature muscle marker (Fig. 2F). Additionally, we tested the effects of hypoxia exposure prior to placement in differentiation media, as occurs in vivo following ischemic muscle injury. Unexpectedly, myofiber formation was impaired in *Bmal1*$^{-/-}$ myoblasts compared with wild type, and these effects were exaggerated following exposure to hypoxia (Fig. 2G,H). Together, our data indicate that although loss of *Bmal1* in myoblasts leads to transcriptional changes associated with the promotion of myoblast differentiation, this is insufficient to drive proper myogenesis, and other clock-regulated factors must be required for hypoxia-specific myogenic cell fate specification.

BMAL1 controls metabolic gene expression and glycolysis in primary myoblasts

RNA sequencing of wild-type and *Bmal1*$^{-/-}$ myoblasts (Fig. 2B) revealed many gene pathways associated with metabolic pathways, such as glycolysis and fatty acid utilization that are *Bmal1*-dependent (Fig. 3A). In hypoxia, *Bmal1*$^{-/-}$ myoblasts displayed reduced expression of genes encoding glucose transport and glycolytic proteins. These genes include several known direct targets of HIF1α, including *Hk2* and *Glut1* (*Slc2a1*), which encode the first enzyme in glycolysis and a glucose transporter, respectively (Fig. 3A [cluster C], B; Supplemental Fig. S6A,B), suggesting that *Bmal1*$^{-/-}$ myoblasts may experience defective glucose utilization during hypoxia due to impaired induction of HIF1α target genes. Indeed, like what we previously observed in mature muscle (Peek et al. 2017), HIF1α protein was reduced in *Bmal1*$^{-/-}$ myoblasts following exposure to hypoxia (Supplemental Fig. S6C).

To directly test whether *Bmal1*$^{-/-}$ myoblasts display impaired function at the level of glucose utilization we performed measurements of extracellular medium acidification rate (ECAR) and oxygen consumption rate (OCR)—readouts of lactate production and mitochondrial respiration, respectively—under high glucose concentrations. We observed impaired OCR and ECAR in *Bmal1*$^{-/-}$ myoblasts compared with wild type. Importantly, the ECAR defect was exaggerated in *Bmal1*$^{-/-}$ myoblasts treated with cobalt chloride ($CoCl_2$), a "hypoxia mimetic" that stabilizes HIF1α (Fig. 3C). These findings, together with our transcriptomic data, demonstrate a hypoxia-specific defect in HIF-dependent glucose utilization in *Bmal1*$^{-/-}$ myoblasts.

In contrast to impaired glycolysis, we observed a hypoxia-specific increase in expression of the fatty acid transporter *Slc27a1* and the pyruvate dehydrogenase complex (PDC) suppressor *Pdk4* in *Bmal1*$^{-/-}$ myoblasts (Fig. 3B; Supplemental Fig. S6B). As up-regulation of both *Pdk4* and *Slc27a1* has been shown to promote fatty acid oxidation (FAO) (Sebastián et al. 2009; Pettersen et al. 2019), we next compared the capacity of wild-type and *Bmal1*$^{-/-}$ myoblasts to oxidize fatty acids using OCR measurements in the presence of the long chain fatty acid palmitate. *Bmal1*$^{-/-}$ myoblasts displayed increased OCR in the presence of exogenous palmitate versus wild-type cells, which was more prominent under hypoxia (Fig. 3D). The induction of RNAs encoding genes that provide FAO substrate together with relative preservation of oxidative versus glycolytic metabolism by cellular bioenergetics indicates a switch in *Bmal1*$^{-/-}$ myoblasts from glucose to fatty acids during hypoxia. Consistent with this, we observed increased phosphorylation at Thr172 of the AMPK α subunit, a known nutrient stress sensor and regulator of metabolic fuel selection (Supplemental Fig. S6D), indicating activation of AMPK activity (Herzig and Shaw 2018). We also observed reduced total ATP and increased AMP/ATP ratio in *Bmal1*$^{-/-}$ myoblasts as well as phosphorylation of Ser79 of acetyl-CoA carboxylase (ACC), a target of AMPK and key enzyme in the switch between fatty acid oxidation and synthesis (Fig. 3E; Supplemental Fig. S6D).

An important metabolic adaptation to hypoxia is the production of lactate from glycolysis-derived pyruvate via the enzyme lactate dehydrogenase A (*Ldha*). This reaction regenerates the cytosolic NAD^+ pool necessary to maintain the glycolytic flux. Consistently, anaerobic

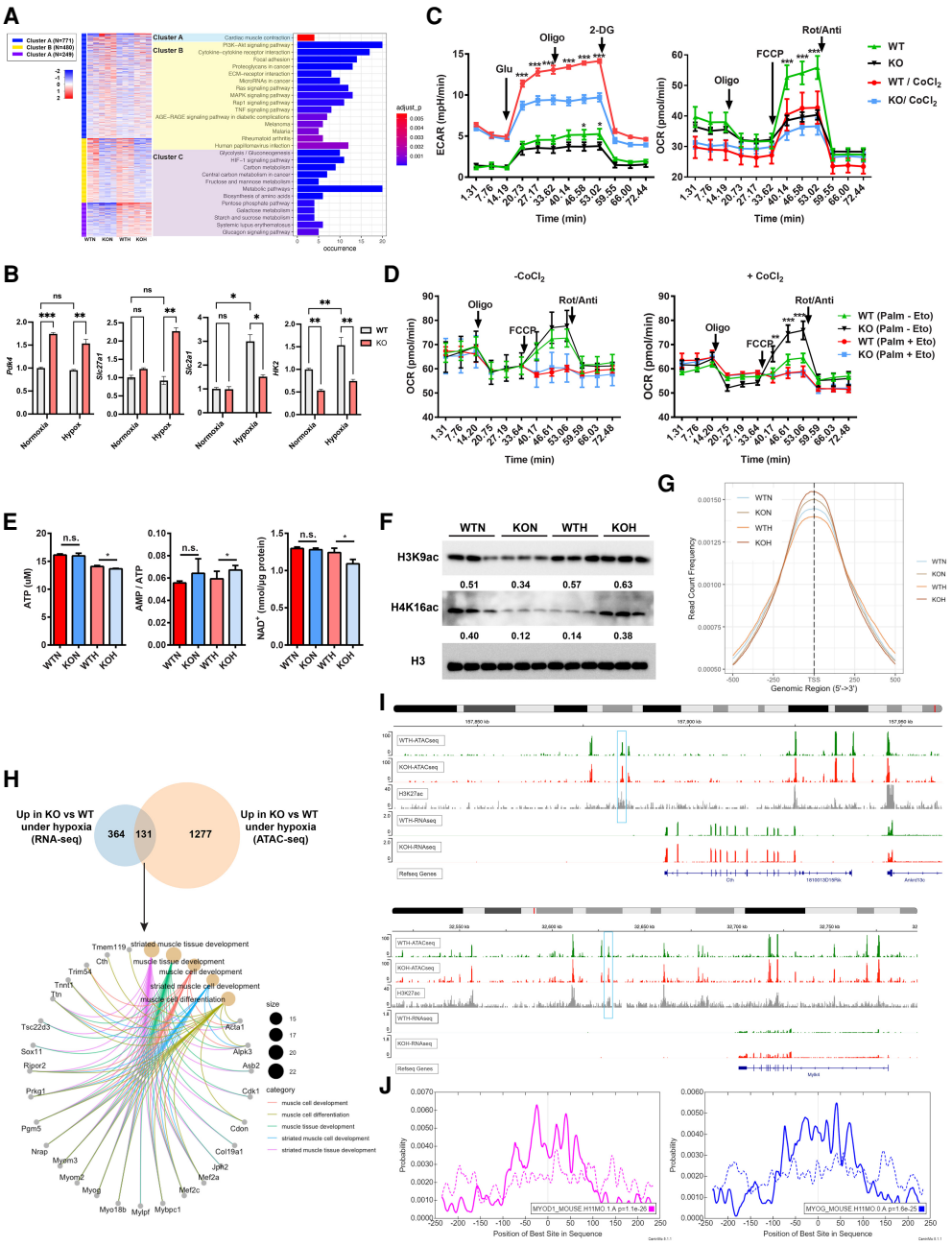

Figure 3. The myoblast circadian clock controls glycolytic and oxidative fuel selection. (*A*) KEGG pathway k-means clustering and enrichment analysis using integrated differential expression and pathway analysis (iDEP) demonstrating enrichment in metabolic pathways in DEGs between *Bmal1*$^{-/-}$ (KO) and WT myoblasts. (*B*) qPCR quantification of DEGs involved in metabolic pathways such as glycolysis and FAO. (*) $P < 0.05$, (**) $P < 0.01$, (***) $P < 0.001$ by two-way ANOVA with Tukey's multiple comparisons test. (n.s.) Nonsignificant. (*C*, *left* graph) ECAR from WT and *Bmal1*$^{-/-}$ myoblasts treated sequentially with glucose, oligomycin (complex V inhibitor), and 2-deoxyglucose (glycolysis inhibitor). (*Right* graph) OCR from WT and Bmal1$^{-/-}$ myoblasts treated sequentially with oligomycin, FCCP (carbonyl cyanide-p-trifluoromethoxyphenylhydrazone; uncoupling agent), and antimycin A/rotenone (ETC inhibitors). $n = 6$ wells per condition. (***) $P < 0.001$ by two-way ANOVA with Tukey's multiple comparisons test. (*D*) OCR measurements from WT and *Bmal1*$^{-/-}$ myoblasts treated without or with 125 µM CoCl2 for 6 h, followed by palmitate-BSA with either 4 µM etomoxir (FAO inhibitor) or vehicle control. OCR measurements were taken as described in *C*. $n = 6$ wells per condition. (**) $P < 0.01$, (***) $P < 0.001$ by one-way ANOVA with Tukey's test for multiple comparisons. (*E*) Relative ATP, AMP/ATP, and NAD$^+$ contents in WT and *Bmal1*$^{-/-}$ myoblasts cultured in normoxia and hypoxia for 6 h. n=3 wells per condition. (*) $P < 0.05$ by two-sided Student's *t*-test comparing only genotype effect within each oxygen condition. (n.s.) Nonsignificant. (*F*) Immunoblots of histone acetylation at H3K9 and H4K16 in WT versus *Bmal1*$^{-/-}$ myoblasts following 0 and 6 h in hypoxia. Numbers *below* the gel images indicate average band intensity relative to total H3. (N) Normoxia, (H) hypoxia. (*G*) Distribution of read count frequency within TSS regions from ATAC sequencing of WT and *Bmal1*$^{-/-}$ myoblasts. (*H*) Gene ontology biological process analysis using genes that display both increased mRNA expression in *Bmal1*$^{-/-}$ myoblasts versus WT and nearby increases in chromatin accessibility. (*I*) IGV genome browser tracks showing RNA sequencing reads from known myogenic genes and ATAC sequencing reads in nearby enhancer regions. (*J*) CentriMo DNA motif analysis of ATAC sequencing data demonstrating higher frequency of MRF motifs near peak centers in *Bmal1*$^{-/-}$ versus WT myoblasts. Data are represented as mean ± SEM.

glycolysis-related genes, including *Ldha* and the lactate exporter *Mct4*, are induced in MuSCs at the hypoxic stage of regeneration (Supplemental Fig. S4C; Latroche et al. 2017). Therefore, we hypothesized that the ECAR defect in *Bmal1*$^{-/-}$ myoblasts (Fig. 3C) results in lower levels of cytosolic NAD$^+$. Indeed, using high-performance liquid chromatography (HPLC) we observed significantly lower total NAD$^+$ levels in *Bmal1*$^{-/-}$ myoblasts compared with controls (Fig. 3E), indicating compromised NAD$^+$ regeneration and energetic balance.

In addition to redox balance, cyto/nuclear NAD$^+$ serves as a cosubstrate for the class III histone deacetylase Sirtuin 1 (SIRT1), which catalyzes the deacetylation of histone lysines (Imai et al. 2000; Landry et al. 2000; Tanno et al. 2007; Zhang and Kraus 2010) and promotes a switch to mitochondrial respiration under low nutrient conditions. Therefore, we assessed the effects of *Bmal1* loss on histone acetylation in myoblasts. *Bmal1*$^{-/-}$ myoblasts displayed increased acetylation of two known SIRT1 target lysines on histone H3 (K27) and H4 (K16) (Vaquero et al. 2007), consistent with lower SIRT1 activity compared with wild-type controls (Fig. 3F). Importantly, these differences were most apparent in cells grown in hypoxia, consistent with the increased reliance on anaerobic glycolysis and cytosolic NAD$^+$ production. Together, these data point toward altered epigenetic regulation of *Bmal1*$^{-/-}$ myoblasts due to impaired hypoxic NAD$^+$ regeneration.

As histone acetylation is generally considered a mark of open chromatin that occurs at the enhancers and transcriptional start sites (TSSs) of transcriptionally active or poised genes (Wang et al. 2008; Barnes et al. 2019), we next asked whether loss of *Bmal1* leads to altered chromatin landscape consistent with the prodifferentiation transcriptomic signature (Fig. 2B). Using assay for transposase-accessible chromatin (ATAC) sequencing, we profiled sites of differential epigenetic regulation between *Bmal1*$^{-/-}$ and wild-type myoblasts in normoxia and hypoxia. We observed increased overall chromatin accessibility surrounding TSS regions in *Bmal1*$^{-/-}$ versus wild-type myoblasts (Fig. 3G; Supplemental Table S1). Furthermore, integration of ATAC and RNA sequencing data showed that the genes with increased chromatin accessibility in their TSS regions displayed higher mRNA levels in *Bmal1*$^{-/-}$ myoblasts versus wild type. Gene ontology analysis of these genes revealed enrichment of muscle lineage differentiation pathways in *Bmal1*$^{-/-}$ myoblasts (Fig. 3H). Furthermore, the regions of open chromatin in *Bmal1*$^{-/-}$ cells include previously annotated enhancer regions, identified by the presence of H3K27ac (Blum et al. 2012), which promote the transcription of genes that facilitate myogenesis in injured muscle (e.g., Cystathionin γ-lyse [*Cth*]) (Zhang et al. 2021) or participate in early myogenesis (e.g., *Mylk4*) (Fig. 3I; Shang et al. 2020). Finally, using Centrimo DNA motif analysis of chromatin-accessible sites (Bailey and Machanick 2012), we observed an enrichment of promyogenic transcription factor motifs in *Bmal1*$^{-/-}$ myoblasts, including MYOD1 and MYOG sites (Fig. 3J).

Our myoblast data suggest that clock mutant myoblasts display impaired glucose utilization and NAD$^+$ regeneration as well as a shift toward fatty acid oxidation. These changes are atypical for proliferating myoblasts that normally retain their anaerobic glycolytic capacity and eventually shift toward pyruvate entry into mitochondria (Ly et al. 2020; Relaix et al. 2021). Consequently, we predict that increased histone acetylation due to lower intracellular NAD$^+$ and SIRT1 activity might lead to inappropriate transcriptional induction of a prodifferentiation gene program in *Bmal1*$^{-/-}$ myoblasts, leading to arrested growth and reduced expansion of myonuclei during hypoxia.

BMAL1 controls activated MuSC proliferation and glucose metabolism following muscle injury in vivo

We next sought to address whether *Bmal1*-dependent coupling of transcription and metabolism mediates muscle injury repair in vivo. In support of this, FACS-based cell quantification demonstrated that while quiescent satellite cell (QSC) numbers were unchanged with loss of MuSC *Bmal1* in uninjured TA muscle, there were significantly fewer ASCs in *Bmal1*^{musc} TA muscle at 3 dpi compared with wild type (Fig. 4A), supporting impaired cell proliferation during the "hypoxic window" postinjury. Next, we performed RNA sequencing of activated MuSCs (ASCs) isolated from TA muscle at day 3 post-CTX-mediated injury (3 dpi)—a time point that coincides with the peak of myogenic cell proliferation (Fig 4B; Supplemental Fig. S7; Liu et al. 2015). Similar to our findings in myoblasts (Fig. 2C,D), loss of ASC *Bmal1* results in reduced enrichment of genes involved in the positive regulation of cell cycle and increased expression of genes that promote ASC myogenesis (Fig. 4C). Interestingly, expression of the cell surface sialomucin factor CD34, which promotes SC proliferation (Alfaro et al. 2011), was reduced in *Bmal1*-deficient ASCs compared with control (Fig. 4D). Low levels of CD34 expression were shown to indicate a "primed" stem cell state that is committed to myogenic differentiation (García-Prat et al. 2020). Additionally, the fatty acid transporter protein CD36 was highly induced in *Bmal1*$^{-/-}$ ASCs (Fig. 4D), consistent with increased fatty acid transporter expression in *Bmal1*$^{-/-}$ myoblasts (Fig. 3B). Gene ontology analysis also revealed increased fatty acid metabolism-related genes in *Bmal1*$^{-/-}$ ASCs, including several components of the β-oxidation pathway (e.g., *Cpt1*, *Cpt2*, *Acads*, and *Ech1*) (Fig. 4E). Furthermore, the previously reported autophagy enhancer Neuropilin2 (*Nrp2*) (Stanton et al. 2013) was decreased while the suppresser NADPH oxidase 2 (*Nox2*, also called *Cybb*) (Pal et al. 2016) was increased in *Bmal1*$^{-/-}$ ASCs compared with control cells (Fig. 4D), suggesting reduced autophagic function in ASCs upon loss of *Bmal1*. Together, these data reveal a role of the MuSC circadian clock in ASC proliferation through regulation of metabolic, proteostasis, and myogenic gene expression during the hypoxic "window" following muscle injury in vivo.

From our myoblast data, we predicted that the clock regulates cell proliferation and myogenesis through control of the metabolic adaptation to hypoxia, which is believed to occur rapidly (<1 h) after CTX injection due to rapid destruction of myofibers and muscle structure

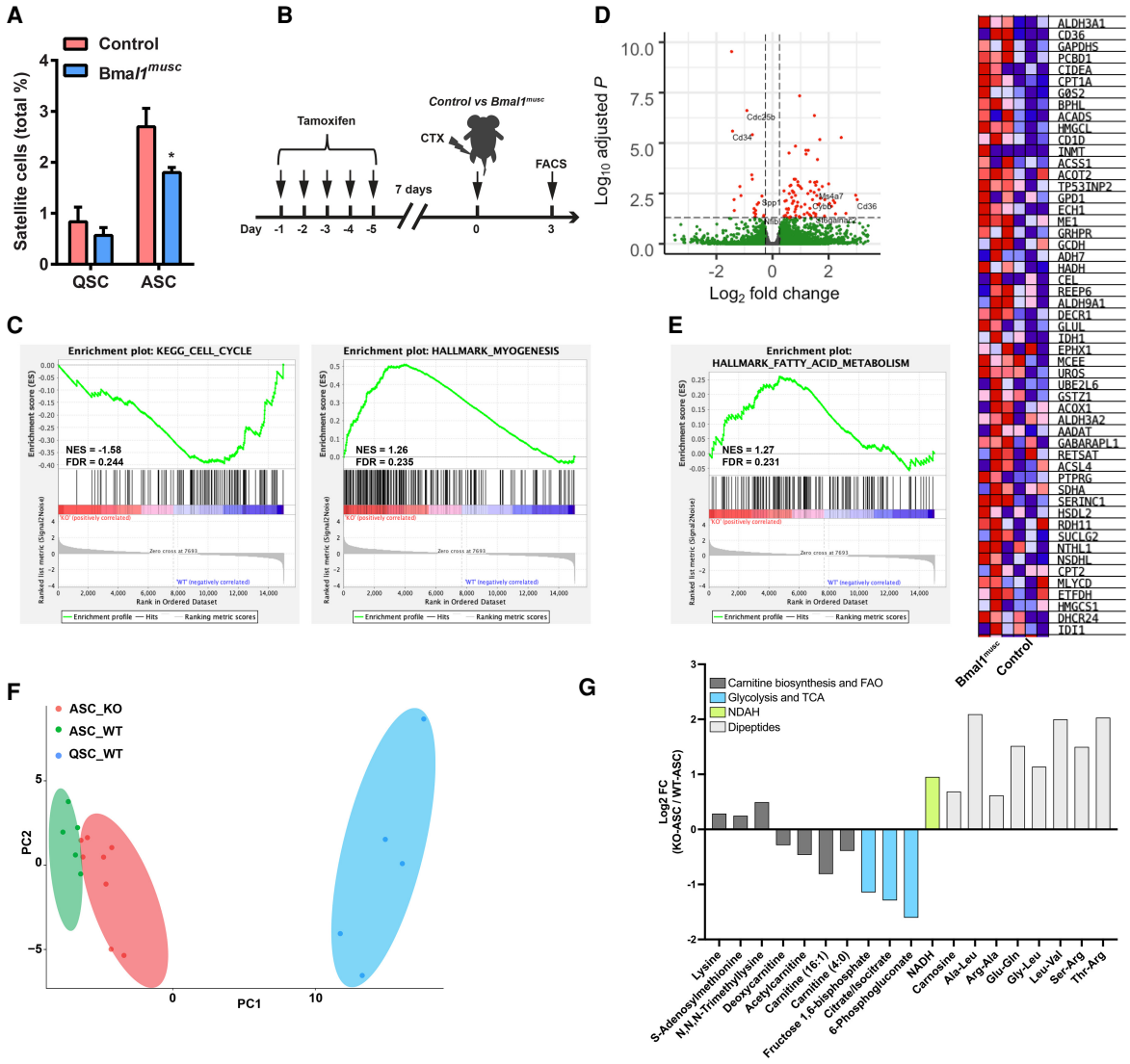

Figure 4. MuSC clock regulates in vivo ASC proliferation as well as glucose and protein metabolism following injury. (*A*) FACS quantification of quiescent (from uninjured TAs) and activated (from TAs at 3 dpi) stem cells isolated from *Bmal1*^{musc} and control mice. (*) $P < 0.05$ by unpaired Student's *t*-test comparing the difference between *Bmal1*^{musc} and control SCs under a given status. (*B*) Experimental design: *Bmal1*^{musc} and control mice received five consecutive daily intraperitoneal injections of 100 mg/kg tamoxifen in corn oil. After 7 d, mice were injected in the TA muscles with CTX, and ASCs were isolated for RNA sequencing at 3 dpi. $n = 5$ mice per genotype. (*C*) GSEA plot of enrichment of cell proliferation- and myogenesis-related genes among DEGs from *Bmal1*^{musc} and control ASCs. (*D*) Volcano plot showing 23 down-regulated and 89 up-regulated genes in *Bmal1*^{musc} ASCs compared with controls at 3 dpi. (*E*) GSEA plot showing enrichment and heat map of fold change of fatty acid metabolism-related genes in *Bmal1*^{musc} and control ASCs. (*F*) PCA plot demonstrating distinct metabolite profiles upon stem cell activation and loss of *Bmal1*. $n = 5$ control, $n = 8$ *Bmal1*^{musc} mice. (*G*) Quantification of significantly ($P < 0.05$) different metabolites between *Bmal1*^{musc} and control ASCs at 3 dpi. Data are represented as mean ± SEM.

(Mahdy et al. 2016). To test this, we sought to directly assess the impact of clock disruption on ASC metabolism following muscle tissue injury. A major limitation of stem cell research is the technical difficulty associated with the measurement of metabolites in rare cell populations (Perez-Ramirez and Christofk 2021). To overcome this problem, we adapted a recently developed method by DeVilbiss et al. (2021) to profile metabolite content in as little as 10,000 freshly isolated MuSCs. Metabolite extraction was done immediately after FACS isolation of ~10,000 QSCs from intact muscles and ASCs from injured muscles on day 3, followed by LC-MS quantification of known metabolites (Fig. 4F; Supplemental Fig. S8A). We assessed metabolite concentrations in MuSCs taken from wild-type and *Bmal1*$^{-/-}$ mice at 3 dpi (Fig. 4B). Of the 250 metabolites detected in both wild-type and *Bmal1*$^{-/-}$ ASCs, 42 (16.8%) of them were significantly different in abundance between the two genotypes (Supplemental Fig. S8B). Strikingly, 33 of these 42 (78.6%) metabolites were also significantly changed between

wild-type QSCs and ASCs, indicating clock regulation of key metabolic pathways altered during MuSC activation. *Bmal1*$^{-/-}$ ASCs displayed reduced levels of glycolytic intermediates (fructose 1,6-bisphosphate and 6-phosphogluconate), TCA cycle intermediates (citrate/isocitrate), and fatty acid metabolites, including acyl-carnitines (Fig. 4G). Similar to what we observed in myoblasts, these data demonstrate altered glucose and fatty acid metabolism in *Bmal1*$^{-/-}$ ASCs following in vivo muscle injury.

We also observed an increase in dipeptide intermediates in *Bmal1*$^{-/-}$ ASCs compared with wild type (Fig. 4G), which might be tied to reduced or impaired autophagic function in the absence of *Bmal1*. Interestingly, autophagy was previously shown to be induced in wild-type ASCs between 1.5 and 5 d after muscle injury (Tang and Rando 2014), and our in vivo muscle stem cell LC-MS data demonstrate that many of the altered dipeptides in *Bmal1*$^{-/-}$ ASCs are lower in wild-type ASCs (at 3 d postinjury) versus QSCs (Supplemental Fig. S8C). This may suggest that the increase in dipeptide intermediates in *Bmal1*$^{-/-}$ ASCs are tied to reduced or impaired autophagic function.

Pyruvate supplementation restores hypoxic growth and myogenic capacity in Bmal1$^{-/-}$ *myoblasts*

Glucose metabolism has been shown to be an essential driver of MuSC fate and function through regulation of histone acetylation (Ryall et al. 2015; Yucel et al. 2019). Thus, we hypothesized that the MuSC clock might regulate myogenic gene transcription and cell fate through the control of glycolysis and NAD^+-regeneration during the hypoxic stage following injury. To test this, we assessed whether rescue of the glycolytic product, pyruvate, could repair defects of *Bmal1* loss on myoblast hypoxic growth and myogenesis (Fig. 5A). *Bmal1*$^{-/-}$ myoblasts cultured in growth medium containing only glucose as a carbon substrate displayed a dramatic reduction in hypoxic growth (Fig. 5B), which was significantly rescued by addition of 2 mM pyruvate to the myoblast growth medium. Additionally, pyruvate supplementation also restored myofiber formation in myoblasts exposed to hypoxia prior to differentiation (Fig. 5C,D). The effect of pyruvate on *Bmal1*$^{-/-}$ myoblast growth and myogenesis was not abrogated in the presence of UK5099, an inhibitor of the mitochondrial pyruvate transport carrier (MPC) (Bricker et al. 2012), suggesting that pyruvate entry into mitochondria is not required to enhance pyruvate-dependent *Bmal1*$^{-/-}$ myoblast growth (Fig. 5B–D). Furthermore, acetate, which can be readily converted to acetyl-CoA in a number of cell types, including stem cells (Moussaieff et al. 2015), only slightly restored myoblast growth and myofiber formation in *Bmal1*$^{-/-}$ myoblasts, indicating that loss of pyruvate-derived acetyl-CoA production may not underlie the growth and differentiation defects (Supplemental Fig. S9A–C). However, addition of α-ketobutyrate (AKB), a four-carbon metabolite that serves as a substrate for LDH-mediated regeneration of cytosolic NAD^+ from NADH (Sullivan et al. 2015), also restored proliferation and differentiation of *Bmal1*$^{-/-}$ myoblasts grown in hypoxia (Fig. 5B–D). Supplementation of nicotinamide mononucleotide (NMN), the product of the NAD^+ salvage biosynthetic enzyme NAMPT, also had a partial effect, again suggesting that NAD^+ deficiency underlies the proliferation and differentiation defects of *Bmal1*$^{-/-}$ myoblasts in hypoxia (Supplemental Fig. S9D–F). Finally, lentiviral delivery of a water-forming NADH oxidase from *Lactobacillus brevis* (*Lb*NOX) (Titov et al. 2016), which serves as a genetic tool for inducing a cytosolic conversion of NADH to NAD^+, also restored hypoxic proliferation and differentiation following growth in hypoxia of *Bmal1*$^{-/-}$ myoblasts (Fig. 5E–G).

Cytosolic NAD(H) cycling can regulate the activity of the NAD^+-dependent deacetylase Sirtuin 1 (SIRT1) (Levine et al. 2021). Therefore, we hypothesized that NAD^+-dependent histone deacetylation might underlie the proliferative and myogenic defects we observed with *Bmal1* loss in myoblasts. To test this, we assessed whether cytoplasmic *Lb*NOX could restore histone deacetylation in *Bmal1*$^{-/-}$ cells. Consistent with raised cytonuclear NAD^+, we observed a reduction of both H3K9 and H4K16 acetylation in *Bmal1*$^{-/-}$ myoblasts with *Lb*NOX expression (Supplemental Fig. S9E). Taken together, these data demonstrate a role for clock-dependent pyruvate production and NAD^+ regeneration in the hypoxic proliferation of myoblasts and ultimate differentiation into myotubes. Our findings emphasize the importance of assessing myoblast proliferation under hypoxia, which provides a permissive environment to support myogenic progenitor proliferation while preventing premature differentiation through clock-controlled glucose metabolism.

Discussion

While studies have reported on the transcriptomic role of cell type-specific clocks, there has been a gap in knowledge concerning the role of circadian clocks in the control of cell identity and progression through developmental programs. Since oxygen sensing is important for cell fate determination in a number of systems (Ezashi et al. 2005; Yang and Levison 2006; Ji et al. 2009; Eliasson and Jönsson 2010), the established connection between clock and hypoxia transcription pathways poses an unexplored connection between circadian timing and cell development. Previous work has demonstrated clock regulation of myoblast differentiation and muscle repair, indicating a role for BMAL1 in the regulation of satellite cell expansion (Andrews et al. 2010; Zhang et al. 2012; Chatterjee et al. 2013, 2015; Solanas et al. 2017; Katoku-Kikyo et al. 2021). However, how intrinsic MuSC clocks direct gene expression changes following injury to promote cell proliferation and differentiation is not understood. Here, we reveal a novel developmental stage-specific role for the molecular clock in adult muscle stem cell metabolic flexibility and epigenetic control of cell fate in response to hypoxic stress following injury.

Metabolic flexibility enables MuSCs to adapt to the changing nutrient environments throughout muscle regeneration and is intimately tied to epigenetic state and

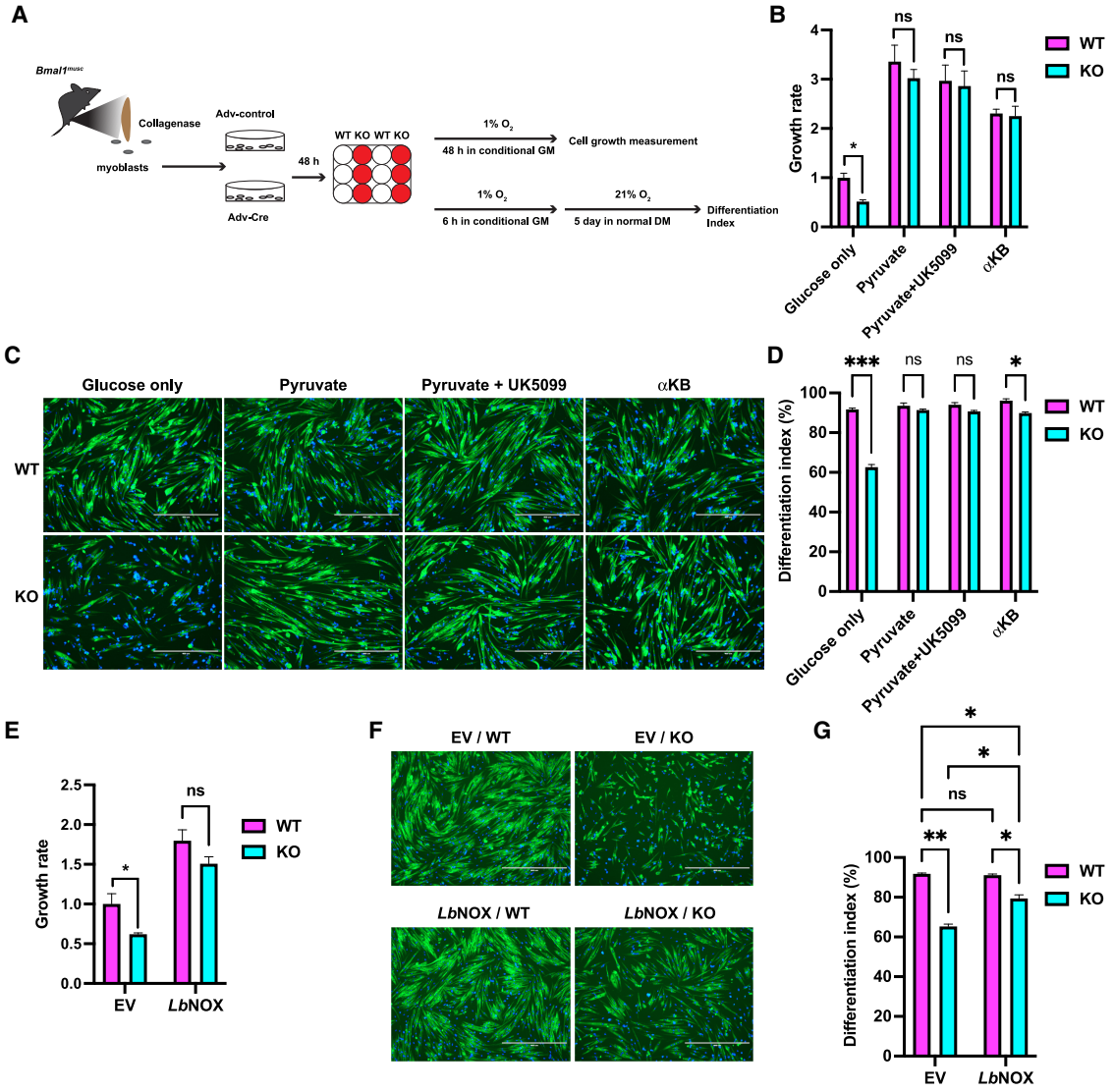

Figure 5. Pyruvate supplementation or NAD^+ replenishment restores hypoxic growth and myogenesis in *Bmal1*$^{-/-}$ myoblasts. (*A*) Experimental design: Primary myoblasts isolated from *Bmal1*^{musc} mice were infected with control (Adv-control) or Cre-expressing (Adv-Cre) adenovirus for 48 h to induce deletion of the *Bmal1* gene. Myoblasts were cultured in "conditional" growth medium (GM) with the indicated nutrients and/or drugs for either 48 h in 1% O2 for cell growth measurements (*top*) or 6 h in 1% O_2 before changing to differentiation medium (DM) in normoxia to allow for myogenic differentiation (*bottom*). (*B*) Cell number quantification by hemocytometer of WT and *Bmal1*$^{-/-}$ (KO) primary myoblasts after culturing in hypoxia for 48 h. (*) $P < 0.05$ by multiple unpaired Student's *t*-tests. (*C*,*D*) MHC and DAPI staining (*C*) and quantification of differentiation index (percentage of MHC$^+$ nuclei) following hypoxic pretreatment under the indicated conditions (*D*; as described in *A*). (*) $P < 0.05$, (***) $P < 0.001$ by multiple unpaired Student's *t*-tests. Scale bar, 400 µm. (*E*) Cell number quantification by hemocytometer of WT and *Bmal1*$^{-/-}$ (KO) primary myoblasts with or without overexpression of *Lb*NOX after culturing in hypoxia for 48 h. (*) $P < 0.05$ by multiple unpaired Student's *t*-tests. (n.s.) Nonsignificant. (*F*,*G*) MHC and DAPI staining (*F*) and quantification of differentiation index in WT and *Bmal1*$^{-/-}$ primary mouse myoblasts with or without overexpression of *Lb*NOX (*G*; as described in *A*). (*) $P < 0.05$, (**) $P < 0.01$ by two-way ANOVA with Tukey's multiple comparisons test. (EV) Empty plasmid vector. Data are represented as mean ± SEM.

cell fate. For example, MuSCs in noninjured muscle favor mitochondrial FAO, and SIRT1 is required to maintain a deacetylated state at histone H4 lysine 16 to keep myogenic genes silent (Ryall et al. 2015). When activated upon injury, MuSCs enter the cell cycle and induce pathways associated with glucose import and glycolysis (Ryall et al. 2015; L'honoré et al. 2018; Pala et al. 2018). Two major products of glycolysis include lactate (anaerobic glycolysis) and acetyl-CoA (aerobic glycolysis), and MuSC acetyl-CoA production has been proposed to drive histone acetylation (Yucel et al. 2019). However, these studies were performed in normoxic conditions, and our data demonstrate that lactate production is increased during hypoxic myoblast proliferation, indicating a switch

toward anaerobic glycolysis. Additionally, proliferation in hypoxia and myogenesis are not restored in *Bmal1*$^{-/-}$ myoblasts with acetate supplementation, which should increase cellular acetyl-CoA and histone acetylation. Instead, raising cytosolic NAD^+ levels—a necessary feature of anaerobic glycolysis—is sufficient to rescue *Bmal1*$^{-/-}$ myoblast proliferation in hypoxia and downstream myogenesis. Therefore, we predict that clock regulation of anaerobic glycolysis and cytosolic NAD^+ acts to regulate SIRT1 deacetylase activity and the genomic maintenance of myoblast cell identity during the "hypoxic window" postinjury. Interestingly, NAD^+ biosynthesis has previously been shown to be important for muscle strength, endurance, and development (Frederick et al. 2016; Basse et al. 2021), as well as MuSC numbers (Zhang et al. 2016). Future studies will be important to uncover whether NAD^+ biosynthesis is also under control of the MuSC clock and is important for muscle regeneration.

Muscle injury is usually accompanied by a rupture of blood vessels, resulting in ischemia and sharp lowering of regional O_2 concentration. A previous study investigating the influence of muscle injury on local vasculature showed an initial destruction of the capillary network followed by angiogenesis and complete regeneration 1 mo after CTX-mediated injury (Hardy et al. 2016). Depending on the type of injury, the duration of local hypoxia is ~4–10 d (Józsa et al. 1980; Kang et al. 2013; Scheerer et al. 2013), with a peak of HIF1α mRNA and protein at ~3.5 dpi in CTX-injured muscles (Drouin et al. 2019). This transient low O_2 state seems to provide a permissive environment for MuSC activation, proliferation, and subsequent differentiation (Urbani et al. 2012; Scheerer et al. 2013; Jash and Adhya 2015; Cirillo et al. 2017). Nevertheless, myogenesis studies often use cultured myoblast models and frequently ignore this transient "hypoxic window" that occurs in the in vivo setting. This is especially important for *Bmal1* in view of its role in the metabolic adaptation in hypoxia (Peek et al. 2017; Wu et al. 2017). Indeed, our studies reveal that *Bmal1*$^{-/-}$ myoblasts exhibit reduced hypoxia-dependent metabolic gene expression as compared with wild type (e.g., *Hk2* and *Glut1*), as well as impaired anaerobic glycolysis and growth in hypoxic conditions. These data demonstrate a role for the circadian clock in activated MuSC adaptation to hypoxic environments and propose that this underlies the impaired muscle regeneration observed in *Bmal1*^{musc} mice.

Our transcriptomic and epigenetic profiling approaches unexpectedly revealed that loss of *Bmal1*$^{-/-}$ in myoblasts displayed increased expression of genes required for myoblast differentiation compared with controls, even under hypoxia when these pathways are normally suppressed. *Bmal1*$^{-/-}$ myoblasts display increased chromatin accessibility surrounding MRF binding sites, including MyoD and myogenin, again supporting a promyogenic transcriptional and epigenetic state. One reason for this could be premature activation of MRFs, and previous studies have shown conflicting results on the effect of *Bmal1* loss on MRF expression (e.g., *Myf5*, *MyoD*, and *myogenin*) (Andrews et al. 2010; Chatterjee et al. 2013). Indeed, our RNA sequencing data revealed that *MyoD* mRNA expression remained unchanged while both *Myf5* and *Myogenin* were significantly up-regulated in *Bmal1*$^{-/-}$ myoblasts compared with wild type, suggesting that loss of *Bmal1* leads to a transcriptionally and epigenetically differentiation-prone state. Notably, a recent study demonstrated an overall reduction in histone acetylation, including H3K9, H3K18, H4K16, and H2BK5 in $Pax7^-MyoD^+$ differentiating progenitors compared with $Pax7^+MyoD^+$-activated MuSCs (Yucel et al. 2019). This and other studies (Francetic et al. 2012; Hamed et al. 2013) have described site-specific increases in histone acetylation and chromatin accessibility around myogenic genes during differentiation. In line with this, our ATAC sequencing data revealed enriched MyoD and myogenin binding motifs in the open chromatin sites specific to *Bmal1*$^{-/-}$ myoblasts, again pointing toward a bona fide state of premature differentiation. Surprisingly however, we did not observe enhanced myofiber formation in cultured *Bmal1*$^{-/-}$ myoblasts, and instead they are impaired for differentiation, particularly following myoblast exposure to hypoxia, suggesting that other mechanisms render them incompetent for myogenesis.

Our transcriptomic results also indicate that *Bmal1*$^{-/-}$ myoblasts are deficient for glycolysis compared with wild type, and this effect is enhanced in hypoxia. We therefore hypothesized that the hypoxia-specific myoblast growth and differentiation defects are tied to an inability of *Bmal1*$^{-/-}$ myoblasts to adapt to increased glucose demand when oxygen is limiting. Interestingly, glycolytic gene expression is regulated by the HIF1α pathway in many cell types, including skeletal muscle and myoblasts (Mason and Johnson 2007; Sakagami et al. 2014), and our data indicate that *Bmal1*$^{-/-}$ myoblasts display reduced hypoxic HIF1α protein accumulation and expression of canonical HIF1α targets, including those involved in glucose metabolism (*Hk2* and *Glut1*). Together, these data lead us to speculate that the impaired HIF1α-mediated oxygen-sensing pathway may, at least in part, underlie the hypoxic growth defect of *Bma1*$^{-/-}$ myoblasts.

While metabolic regulation is an important factor in MuSC maintenance and differentiation, there remains a major challenge in stem cell metabolite profiling due to their low abundance (Perez-Ramirez and Christofk 2021). Here, we have performed the first, to our knowledge, metabolomic profiling study of ~10,000 MuSCs taken directly from mouse muscle tissue both preinjury and postinjury. By comparing metabolites enriched in activated versus quiescent MuSCs, we detected many intermediate metabolites in glycolysis, TCA, and FAO that would be predicted from transcriptomic studies performed in these cell types (Pala et al. 2018), thus validating the utilization of this novel untargeted metabolomic method. Consistent with our ASC and myoblast RNA sequencing data, we observed a reduction in glycolytic and TCA cycle intermediates in ASCs from *Bmal1*^{musc} mice at 3 dpi compared with control, indicating impaired glycolysis. Strikingly, we also observed an accumulation of dipeptides in *Bmal1*$^{-/-}$ ASCs. Further investigation is required to determine whether this is tied to the incomplete autophagy-mediated protein catabolism.

In summary, here we uncovered a novel mechanism connecting circadian clock-controlled metabolism to cell fate and tissue repair. Specifically, we revealed that loss of the MuSC-autonomous clock abrogates metabolic and genomic responses to hypoxia and leads to impaired myogenesis and regeneration. Future work will be required to understand the full scope of clock-controlled muscle repair over the 24-h circadian time scale.

Materials and methods

Mice

C57BL/6J mice and B6.Cg-*Pax7*$^{tm1(cre/ERT2)Gaka}$/J mice were purchased from the Jackson Laboratory. *Bmal1*$^{fx/fx}$ mice (Johnson et al. 2014) with an additional lineage-tracing allele (fx-STOP-fx-tdTomato) (Jackson Laboratories stock no. 007676) were provided by Dr. Joseph Bass at Northwestern University. Muscle stem cell-conditional deletion of *Bmal1* was achieved by crossing *Bmal1*$^{fx/fx}$*tdTomato*$^{fx/fx}$ mice with B6.Cg-*Pax7*$^{tm1(cre/ERT2)Gaka}$/J mice to generate *Bmal1*$^{fx/fx}$*tdTomato*$^{fx/fx}$*Pax7*$^{tm1(cre/ERT2)}$ as well as *Bmal1*$^{+/+}$*tdTomato*$^{fx/fx}$*Pax7*$^{tm1(cre/ERT2)}$ control mice. Loss of Bmal1 was induced by five consecutive daily intraperitoneal injection of 20 mg/mL tamoxifen (100 mg/kg body weight; Sigma T5648) in corn oil. Mice were maintained on a 12:12 light:dark cycle. All experiments were performed using 8- to 12-wk-old male mice and following the guidelines of the Institutional Animal Care and Use Committee at Northwestern University.

Skeletal muscle injury

Cardiotoxin-mediated tibialis anterior (TA) muscle injury was adapted from previously described methods (Zhu et al. 2019). Mice were anesthetized by intraperitoneal injection of a ketamine (80 mg/kg) and xylazine (10 mg/kg) cocktail. After shaving the skin hair, TA muscles were injected with 50 µL of 10 µM working solution of cardiotoxin (CTX; Millipore Sigma 217503-1MG) in saline using a 1-mL BD Slip Tip syringe (BD 309623).

Histology

To assess muscle regeneration, TA muscles were dissected at the indicated time points postinjury and wrapped with a thin layer of Tissue-Tek O.C.T. compound (Fisher Scientific). The tissues were then snap-frozen in liquid nitrogen-cooled isopentane and stored at −80°C until analysis. Frozen TAs were cut into continuous 10-µm cross-sections using a Leica CM1860 cryostat. For hematoxylin and eoxin (H&E) staining, the frozen sections were dried overnight at room temperature before staining. After a 5-min rehydration in PBS, the sections were fixed with 10% formalin (Millipore Sigma MR0458682) and then immersed in hematoxylin for 5 min to stain the nuclei. Excessive hematoxylin was washed off by running tap water for 5 min followed by a few quick dips in clarifier (Sigma A3179) for removal of nonnucleus staining in the tissue. The slides were further subjected to 30-sec immersion with eosin solution for cytoplasm and connective tissue staining. After a successive transfer of the slides in gradient ethanol for dehydration and xylene for transparency, the slides were mounted with Permount mounting medium (Electron Microscopy Science 17986-01) and observed using a Keyence BZ-X800 microscope.

Immunohistochemistry

Tissue sections were air-dried for 30 min at room temperature and fixed with 4% paraformaldehyde. After 15-min permeabilization in 0.25% Triton X-100, the sections were blocked for nonspecific binding sites with phosphate-buffered saline (PBS) with 5% goat serum, 2% bovine serum albumin (BSA), and 1% Tween-20 for 1 h followed by overnight incubation with anti-Laminin (1:100 dilution; Sigma-Aldrich L9393) primary antibody in diluent buffer (PBS with 0.5% goat serum, 2% bovine serum albumin, 1% Tween-20) at 4°C. The slides were washed three times with PBS, and the sections were then incubated with Alexa fluor 488-conjugated goat antimouse IgG secondary antibody (1:1000 dilution; Invitrogen A28175) in diluent buffer for 1 h at room temperature. The sections were mounted with VectaShield HardSet antifade mounting medium with DAPI (Vector Laboratories H-1500-10) and observed using a Keyence BZ-X800 microscope. The myofiber CSA was quantified using ImageJ software (https://imagej.nih.gov/ij).

Immunofluorescence

Primary myoblast-derived myotubes were washed once with ice-cold PBS, and fixed with acetone for 15 min at –20°C. The myotubes were then permeabilized with 0.2% Triton X-100 and blocked for nonspecific binding sites using 1% BSA for 1 h at room temperature, followed by an overnight incubation with antimyosin heavy chain antibody (1:50 dilution; DSHB MF20) at 4°C. The cells were washed three times with PBS the next day and incubated with Alexa fluor 488-conjugated goat antimouse IgG secondary antibody (1:1000 dilution; Thermo Fisher Scientific A28175) in 1% BSA for 1 h at room temperature. The nuclei were stained with DAPI (5 µg/mL in PBS) for 5 min followed by fluorescence imaging using an Evos FL cell-imaging microscope (Thermo Fisher Scientific).

Muscle cell isolation

Entire hindlimb (for myoblast cultures) or TA (for RNA and ATAC sequencing as well as metabolomics) muscles were dissected and cleaned by removing nonmuscle tissues and subjected to digestion in Hams F-10 medium (Corning 10-070-CV) containing 5 mg/mL collagenase D (Roche 11088866001) and 5 mg/mL dispase II (Gibco 17105041) for 30 min at 37°C with 500 rpm shaking. The enzymatic digestion was terminated by adding a fivefold volume of ice-cold cell suspension buffer (Ham's F-10 with 10% FBS, 3 mM EDTA). Digested muscle tissue was further mechanically triturated by vigorous passing through a 10-mL pipette (20 times) to release MuSCs from the attached myofibers. The cell suspension was then filtered sequentially through 70- and 40-µm nylon mesh strainers (BD Biosciences), and the flow-through was collected in a 15-mL conical tube and centrifuged at 500×*g* for 5 min. Cell pellets were resuspended in 1 mL of Pre-Sort buffer (BD Biosciences 563503), and Live-or-Dye 640/662-negative (Biotium 32007), tdTomato-positive mononuclear MuSCs were sorted using a BD FACSAria II cell sorter.

Myoblast isolation, culture, and differentiation

Myoblasts were prepared based on a previously described preplating strategy with minor modifications (Gharaibeh et al. 2008). Briefly, muscle tissues were enzymatically digested as described above using collagenase and dispase II. This crude suspension was plated and expanded on a Matrigel-coated (Corning 354277) 60-mm dish in myoblast growth medium (Hams F-10/20% FBS/1% penicillin–streptomycin [PS]/5 ng/mL basic fibroblast growth

factor [bFGF; ProSpec CYT-218]) for 3 d. Cells were then trypsinized and preplated on a regular tissue culture-treated 60-mm dish for 1 h followed by transfer to another Matrigel-coated dish. This passage strategy was repeated three times, at which point the majority of nonmyoblast cells were eliminated. The enriched myoblast cultures were then maintained in DMEM/Hams F-10 (1:1) growth medium containing 20% FBS, 1% PS, and 5 ng/mL bFGF. We confirmed >95% myoblast purity using this method by immunofluorescence using a Pax7-antibody (Developmental Studies Hybridoma Bank). For differentiation, myoblasts were switched from growth medium into the differentiation medium (DMEM/2% horse serum/1% PS) for 3–5 d. All of the loss-of-function assays were performed at least 48 h after infecting primary myoblasts with adenovirus expressing Cre (Adv-Cre) or empty vector (Adv-Ctrl) (Vector Biolabs). Nutrients and chemicals used for myoblast treatment were 2 mM sodium pyruvate (Sigma-Aldrich P5280), 2 mM sodium acetate (Tocris 3159), 1 mM α-ketobutyrate (Sigma-Aldrich K0875), 10 µM UK-5099 (Sigma-Aldrich PZ0160), and 0.5 mM β-nicotinamide mononucleotide (Sigma-Aldrich N3501).

Sample preparation for RNA sequencing

Myoblasts Total RNA from primary myoblasts was isolated using the Direct-zol RNA MicroPrep kit (Zymo Research) and quantified using Qubit RNA BR assay kit (Thermo Fisher Scientific Q10210) for regular RNA sequencing. cDNA libraries were constructed from 1 µg of total RNA using the TruSeq stranded total RNA library preparation kit (Illumina 20020596). DNA fragments in the library were amplified with 15 PCR cycles, size-selected using AMPure XP beads (Beckman Coulter A63880) for enrichment of fragments between 200 and 500 bp, and sequenced on the Illumina NextSeq 500 in a paired-end run (twice for 51 bp) for a sequencing depth of ~30 million reads per sample.

MuSCs Total RNA from FACS-sorted satellite cells was isolated using SMART-seq v4 Ultra low input RNA kit (Takara Bio) for low-input RNA sequencing. One-thousand Live-or-Dye 640/662-negative, tdTomato-positive mononuclear satellite cells were sorted directly into 200-µL conical Eppendorf PCR tubes containing 10× lysis buffer and 3′SMART-seq CDS primer IIA for first strand cDNA synthesis, followed by 10 cycles of PCR amplification and purification using the Agencourt AMPure XP kit (Beckman Coulter A63880). The purified cDNA was analyzed using the Agilent 2100 Bioanalyzer and Agilent's high-sensitivity DNA kit (Agilent 5067-4626). Three-hundred picograms of full-length cDNA from the SMART-seq v4 Ultra low-input RNA kit was processed with the Nextera XT DNA library preparation kit (Illumina FC-131-1024). The PCR-amplified, size-selected cDNA fragments were visualized using the Agilent 2100 Bioanalyzer and Agilent's high-sensitivity DNA kit and quantified using Qubit dsDNA HS assay kit (Thermo Fisher Scientific Q32851). Pooled libraries were sequenced on a Novaseq 6000 instrument (Illumina) in a paired-end run (twice at 51 bp) for a sequencing depth of ~50 million reads per sample.

RNA sequencing analysis

Raw BCL files were converted to demultiplexed, paired-end read FastQ files using bcl2fastq software (v2.19.1). Adaptor sequences were trimmed using the Trimmomatic (v0.33) tool (Bolger et al. 2014), and the trimmed reads were mapped to the mm10 *Mus musculus* reference genome using STAR aligner (v2.5.2) (Dobin et al. 2013). The number of alignments mapped to each gene was counted using RSEM (v1.3.3) (Li and Dewey 2011). The isoform-level RSEM quantifications were passed to DESeq2 (Love et al. 2014) using the tximport package (Soneson et al. 2016) by setting type to "rsem," and "txIn" and "txOut" to "TRUE." When performing differential gene expression analysis on in vitro myoblast sequencing data, the differences in response to treatment between genotypes were taken into consideration by using a design of ~genotype + condition (normoxia versus hypoxia) + genotype:condition. Differentially expressed genes (DEGs) were generated through the results function in DESeq2 and further corrected for multiple testing (an adjusted *P*-value was generated using the Benjamini-Hochberg correction). Gene counts for the differentially expressed genes were visualized using the pheatmap (v1.0.12) and EnhancedVolcano (version 1.2.0) packages in R (v3.6.1). KEGG pathway enrichment and gene ontology analyses were performed using gene set enrichment analysis (Subramanian et al. 2005) for in vivo MuSC analysis, or EnrichR (Kuleshov et al. 2016) and ShinyGO (v0.66) (Ge et al. 2019) for in vitro myoblast analysis. De novo motif discovery was performed on DEGs using the HOMER (v4.10) (Heinz et al. 2010) findMotifs.pl program by searching for motifs of length 6, 8, and 10 bp from −1000 to +500 bp relative the TSS.

Sample preparation for ATAC sequencing

ATAC sequencing methods for myoblasts was adapted from a previously published protocol (Buenrostro et al. 2013). Briefly, myoblasts in six-well plates were washed once with 1× PBS, scraped, and collected in 1.5-mL Eppendorf LoBind microcentrifuge tubes by a 500×*g* centrifugation for 5 min at 4°C. The cells were permeabilized in 50 µL of detergent-added ATAC buffer (DAB; 10 mM Tris-HCl at pH 7.4, 10 mM NaCl, 3 mM $MgCl_2$, 0.1% IGEPAL, 0.1% Tween-20, 0.01% digitonin), followed by a 3-min incubation on ice. One milliliter of ice-cold resuspension buffer with Tween-20 (RSB-T; 10 mM Tris-HCl, 10 mM NaCl, 3 mM $MgCl_2$, 0.1% Tween-20) was added, and tubes were inverted three times to mix. The cell suspension was further passed through a BD insulin needle once to completely lyse the cells and release the nuclei. The density of the resulting nuclear suspension was calculated by hemocytometer counting. A volume corresponding to ~50,000 nuclei was transferred to a new LoBind tube and spun at 500×*g* for 10 min at 4°C to pellet nuclei. After carefully removing the supernatant, the nuclear pellet was resuspended in 50 µL of transposition mixture (Illumina Tagment DNA enzyme and buffer small kit 20034197) with 0.01% digitonin and 0.1% Tween-20 and incubated for 30 min at 37°C in a thermomixer with shaking at 1000 rpm. The tagmented chromatin DNA was purified using Minelute Qiagen cleanup kit (Qiagen 28206), and then subjected to PCR-based indexing and library amplification using NEBNext high-fidelity 2× PCR master mix (NEB M0541). The amplified libraries were size-selected using Pippin Prep (2% gel cassette for 100- to 600-bp fragments) and purified using AMPure XP beads (Beckman Coulter A63880). The libraries were then quantified individually using the NEBNext library Quant kit (NEB E7630) and pooled for sequencing on an Illumina NextSeq 500 in a paired-end run (twice at 51 bp) for a sequencing depth of ~30 million reads per sample.

ATAC sequencing analysis

The paired-end FastQ files were concatenated and the trimmed reads were mapped to the mm10 *Mus musculus* reference genome using Bowtie2 (v2.4.1) (Langmead and Salzberg 2012) with default parameters except for use of the "–very-sensitive" option. The aligned reads were filtered sequentially for mitochondrial DNA (by SAMtools v1.10.1), PCR duplicates (by Picard's

Markduplicates program), and nonunique alignments with mapping quality (MAPQ) score <30 (by SAMtools v1.10.1), and then subjected to peak calling using MACS2 with parameters "-f BAMPE -g mm –keep-dup all." The defined ENCODE blacklist regions were excluded from the called peaks using the BEDtools (v2.29.2) intersect function. Comparison of the average profile of ATAC peak binding from –500 to +500 relative to the TSS was performed using the ChIPseeker (v1.26.2) R package (Yu et al. 2015). Differential accessibility analysis was performed by following the workflow provided in an earlier study (Reske et al. 2020). The identified sites of differential chromatin accessibility were annotated using the HOMER (v4.10) annotatePeaks.pl program. The local enrichment of motifs centered in the input peaks relative to wild-type control under hypoxia condition was identified using the CentriMo online tool (Bailey and Machanick 2012).

Western blotting

Western blotting was performed as previously described (Peek et al. 2017). Briefly, myoblast whole-cell lysates were prepared in CelLytic MT mammalian tissue lysis reagent (Sigma C3228) supplemented with protease inhibitors (Sigma P8340). Each snap-frozen mouse TA muscle was placed in 500 µL of CelLytic MT mammalian tissue lysis reagent supplemented with protease inhibitors and homogenized using a TissueLyser II apparatus (Qiagen). Protein levels were quantified using a DC protein assay (Bio-Rad 5000111), subjected to SDS-PAGE gel electrophoresis, and transferred onto 0.45-µm nitrocellulose membranes (Bio-Rad 1620115). Primary antibodies used were anti-HIF1α (1:1000 dilution; Cayman 10006421), BMAL1 (1:1000 dilution; Cell Signaling 14020), phospho-AMPKα (Thr172; 1:1000 dilution; Cell Signaling 2535), AMPKα (1:1000 dilution; Cell Signaling 5831), phospho-acetyl-CoA carboxylase (Ser79; 1:1000 dilution; Cell Signaling 11818), acetyl-CoA carboxylase (1:1000 dilution; Cell Signaling 3676), Beclin-1 (1:1000; Cell Signaling 3495), LC3A/B (1:1000; Cell Signaling 12741), Atg3 (1:1000; Cell Signaling 3415), Atg5 (1:1000; Cell Signaling 12994), Atg7 (1:1000; Cell Signaling 8558), anti-β-Actin (1:10,000 dilution; Cell Signaling 4970), acetyl-Histone H4 (Lys16; 1:1000 dilution; Cell Signaling 13534), Histone H3 (1:1000; Cell Signaling 4499), and Histone H3 (acetyl K9; 1:1000 dilution; Abcam ab4441).

For histone modifications, total histone extracts were prepared using a histone extraction kit (Abcam ab113476). The histone extracts were subjected to 15% SDS-PAGE and transferred to 0.2-µm nitrocellulose membranes (Bio-Rad 1620112). Primary antibodies used were anti-acetyl-Histone H4 (Lys16; E2B8W; 1:1000 dilution; Cell Signaling 13534), anti-Histone H3 (acetyl K9; 1:1000 dilution; Abcam ab32129), and anti-Histone H3 (D1H2; 1:1000 dilution; Cell Signaling 4499).

Oxygen consumption rate (OCR) and extracellular medium acidification rate (ECAR) measurements

OCR and ECAR were measured in myoblasts as previously described (Peek et al. 2017). Briefly, primary *Bmal1*$^{fx/fx}$ myoblasts were infected with control- or Cre-expressing adenoviruses for 48 h followed by replating in Seahorse XF 96-well culture plates at equal density (2×10^4 cells per well). Cells were allowed to adhere for 2 h and then cultured for 6 h in the absence or presence of 125 µM $CoCl_2$. At the end of treatment, the growth medium was replaced with serum-free Seahorse XF media in the absence (for ECAR) or presence (for OCR) of glucose and equilibrated in a 37°C CO_2-free incubator for 45 min followed by Seahorse measurement. OCR and ECAR were measured before and after sequential ejection of 10 µM oligomycin and 10 µM carbonylcyanide-p-trifluoromethoxyphenylhydrazone (FCCP; for OCR) or 10 mM glucose and 10 µM oligomycin (for ECAR).

Long chain fatty acid oxidation assay (LCFAO)

LCFAO was measured on a Seahorse bioanalyzer using the Seahorse XF palmitate oxidation stress test kit (Agilent 103693-100). Briefly, myoblasts were plated at a density of 20,000 cells/well in 96-well Seahorse culture plates and allowed to attach for 2 h in complete growth medium. Cells were then changed into a substrate-limited growth medium (Seahorse XF DMEM supplemented with 0.5 mM glucose, 1 mM glutamine, 1% FBS, 0.5 mM XF L-carnitine) and incubated overnight. During the last 5 h of this incubation, 125 µM $CoCl_2$ was added to the indicated wells. Media were then replaced with substrate-limited assay media (Seahorse XF DMEM supplemented with 2 mM glucose, 0.5 mM XF L-carnitine) with or without 125 µM $CoCl_2$, and the plate was placed in a non-CO_2 37°C incubator for 1 h. Media were then aspirated and replaced with 150 µL of substrate-limited assay media with either 30 µL of palmitate-BSA or BSA alone. OCR was measured before and after sequential ejection of 4 µM etomoxir, 10 µM oligomycin, and 10 µM FCCP.

Nucleotide measurements

Nucleotide measurements were performed using HPLC as previously described (Peek et al. 2013). Briefly, myoblasts in 60-mm culture dishes were washed once with 1× PBS followed by addition of 300 µL of 10% (1.66 M) perchloric acid (Sigma 244252). The cells were then scraped into 1.5-mL tubes and lysed for 10 min on ice followed by centrifugation at 18,000×*g* for 5 min at 4°C. Supernatant (150 µL) was transferred to a new 1.5-mL tube and neutralized with 50 µL of 3 M K_2CO_3. The tubes were vortexed and incubated for 10 min on ice, followed by a centrifugation at 18,000×g for 5 min at 4°C. One-hundred microliters of supernatant from each tube was transferred to HPLC vials containing 100 µL of 1× phosphate buffer, and NAD^+ and ATP were measured on a Shimadzu LC-20A pump and UV-VIS detector with a Supelco LC-18-T column (15 cm × 4.6 cm). The HPLC was run at a flow rate of 1 mL/min with 100% buffer A (0.5 M KH_2PO_4, 0.5 M K_2HPO_4) from 0 to 5 min, a linear gradient to 95% buffer A/5% buffer B (100% methanol) from 5 to 6 min, 95% buffer A/5% buffer B from 6 to 11 min, a linear gradient to 85% buffer A/15% buffer B from 11 to 13 min, 85% buffer A/15% buffer B from 13 to 23 min, and a linear gradient to 100% buffer A from 23 to 30 min. NAD^+ eluted as a sharp peak at 14 min and was normalized to protein content of cultured cells.

Muscle stem cell metabolomics

For ASC and QSC metabolomics analyses, muscle stem cells were isolated and prepared in a modified protocol to minimize the timing of isolation. MuSCs were collected only from TA muscles that were kept in ice-cold PBS after dissection until digestion. The following procedures were all performed in a 4°C cold room or on ice. Muscles were minced quickly into small pieces in 1× HBSS (Gibco 14185052) containing 10 mg/mL collagenase D (Roche 11088866001) and 10 mg/mL dispase II (Gibco 17105041) for 15 min at 37°C with 1000 rpm shaking. The enzymatic digestion was stopped by adding fivefold volume of 1× HBSS containing 0.5% BSA (Sigma A7906), and the extracts were further mechanically triturated through vigorous passing through a 10-mL pipette prechilled in –20°C (10 times) to release MuSCs from the attached myofibers. The resulting cell

suspension was then filtered through a 40-μm nylon mesh strainer (BD Biosciences), and the flow-through was collected in a 15-mL conical tube and centrifuged at 500×*g* for 5 min at 4°C. The cell pellet was resuspended in 500 μL of sorting medium (1× HBSS/0.5% BSA) containing 1 μL of Live-or-Dye 640/662 (Biotium 32007), and immediately subjected to FACS sorting. Samples were then collected in 1.5-mL Eppendorf tubes (kept very clean to avoid contamination) that were preloaded with 40 μL of ice-cold acetonitrile (Fisher Scientific, Optima) and stored at –20°C until right before sorting. A clean microfuge tube opener (USA Scientific) was used to open and close the tubes in order to minimize chance of contamination from gloves. Ten-thousand Live-or-Dye 640/662-negative and tdTomato-positive MuSCs (~10 μL) were sorted at a flow rate of no more than 4.4 μL/min to reduce the shear stress. The tubes were centrifuged briefly to bring down all the liquid in the bottom and placed on dry ice. Sheath blanks (10 μL of sheath fluid in 40 μL of acetonitrile) and solvent blanks (50 μL of acetonitrile) were prepared as controls to determine the level of metabolite contamination. Metabolites were extracted using a previously described method (DeVilbiss et al. 2021) and analyzed immediately by LC-MS. Liquid chromatography was performed with a Vanquish Flex UHPLC (Thermo Scientific) using a Millipore Sigma ZIC-pHILIC column (2.1 × 150, 5 μm) with a binary solvent gradient composed of water containing 10 mM ammonium acetate (pH 9.8) and 100% acetonitrile. All mass spectrometry data were acquired using a Thermo Scientific QExactive HF-X mass spectrometer operating in polarity-switching MS1-only mode. Each polarity was acquired at a resolving power of 120,000 full width at half maximum (FWHM); and the automatic gain control (AGC) target was set to 1,000,000 with a maximum inject time of 50 msec. The scan range was set to 80–1200 Da. Instrument performance was evaluated before each experiment by analyzing a quality control sample: 20 μL of freshly obtained rat serum.

Technical note on flow cytometer preparation Before each FACS collection, the BD FACSAria II cell sorter was thoroughly cleaned to minimize metabolite contamination. Specifically, a fluidics shutdown protocol was performed after turning on the flow cytometer by connecting an ethanol tank containing 70% ethanol. The ethanol tank was then replaced by a clean, metabolomics-dedicated FACSAria sheath tank that was prerinsed multiple times with ultrapure water and filled with freshly made 0.5× PBS (Sigma 79382) dissolved in ultrapure water, and connected to the sorter using a dedicated 0.22-μm filter. The fluidics startup protocol was performed using 0.5× PBS sheath fluid, followed by two rounds of clean flow cell protocols with Windex that was allowed to sit in the flow cell for 5–10 min after the running the protocol. Steam was then run through the flow cytometer at maximum flow rate (11 μL/min) to flush Windex and any remaining debris in the flow cell. Meanwhile, the 70-μm nozzle was sonicated for 3 min and confirmed by microscopy to be free of debris. Before installing the nozzle, the sort chamber was cleaned with a lint-free wipe and cotton swabs. After inserting the nozzle, 5 mL of Windex was then run at maximum flow rate (11 μL/min) followed by ultrapure water and then steam to clean the sample line. The flow cytometer was set to four-way purity sort mode to minimize droplet size.

Statistical analysis

Statistical analysis was performed by unpaired two-tailed Student's *t*-test in most cases except when otherwise noted in the figure legends. Where appropriate, data are represented as mean ± SEM. Two-way ANOVA was performed to compare the effect of both *Bmal1* expression and *Lb*NOX expression on myoblast differentiation. Differences were considered statistically significant when $P < 0.05$.

Competing interest statement

N.S.C. is on the scientific advisory board of Rafael Pharmaceuticals. The authors declare no other competing interests.

Acknowledgments

We thank Dr. Joseph Bass, Dr. Issam Ben-Sahra, Dr. Elizabeth McNally, Dr. Mattia Quattrocelli, and all members of the Peek, Bass, and Barish laboratories for helpful discussion. This research was supported by National Institutes of Health National Institute of Diabetes and Digestive and Kidney Diseases grants R01DK123358 (to C.B.P.) and F31DK130589 (to N.J.W.); National Heart, Lung, and Blood Institute grant F32HL135975 (to A.W.D.); National Cancer Institute grant R35CA197532 (to N.S.C.); and National Institute on Aging grant P01AG049665 (to N.S.C).

Author contributions: P.Z. and C.B.P. designed the studies. P.Z. performed and analyzed all experiments unless indicated otherwise. N.X.H., A.V.T., N.J.W., E.J.R., A.W.T.S., and N.H.K. provided technical assistance. A.W.D., T.P.M. and M.S.M.-S. performed in vivo MuSC LC-MS and MS analysis. N.S.C. provided *LbNOX* constructs and input on experimental design. C.B.P. and P.Z. wrote the manuscript.

References

Alfaro LAS, Dick SA, Siegel AL, Anonuevo AS, McNagny KM, Megeney LA, Cornelison DDW, Rossi FMV. 2011. CD34 promotes satellite cell motility and entry into proliferation to facilitate efficient skeletal muscle regeneration. *Stem Cells* **29:** 2030–2041. doi:10.1002/stem.759

Andrews JL, Zhang X, McCarthy JJ, McDearmon EL, Hornberger TA, Russell B, Campbell KS, Arbogast S, Reid MB, Walker JR, et al. 2010. CLOCK and BMAL1 regulate MyoD and are necessary for maintenance of skeletal muscle phenotype and function. *Proc Natl Acad Sci* **107:** 19090–19095. doi:10.1073/pnas.1014523107

Bailey TL, Machanick P. 2012. Inferring direct DNA binding from ChIP-seq. *Nucleic Acids Res* **40:** e128. doi:10.1093/nar/gks433

Barnes CE, English DM, Cowley SM. 2019. Acetylation & Co: an expanding repertoire of histone acylations regulates chromatin and transcription. *Essays Biochem* **63:** 97–107. doi:10.1042/EBC20180061

Bass J, Lazar MA. 2016. Circadian time signatures of fitness and disease. *Science* **354:** 994–999. doi:10.1126/science.aah4965

Bass J, Takahashi JS. 2010. Circadian integration of metabolism and energetics. *Science* **330:** 1349–1354. doi:10.1126/science.1195027

Basse AL, Agerholm M, Farup J, Dalbram E, Nielsen J, Ørtenblad N, Altıntaş A, Ehrlich AM, Krag T, Bruzzone S, et al. 2021. Nampt controls skeletal muscle development by maintaining $Ca2^+$ homeostasis and mitochondrial integrity. *Mol Metab* **53:** 101271. doi:10.1016/j.molmet.2021.101271

Beaudry M, Hidalgo M, Launay T, Bello V, Darribère T. 2016. Regulation of myogenesis by environmental hypoxia. *J Cell Sci* **129:** 2887–2896.

Bentzinger CF, Wang YX, Dumont NA, Rudnicki MA. 2013. Cellular dynamics in the muscle satellite cell niche. *EMBO Rep* **14:** 1062–1072. doi:10.1038/embor.2013.182

Blum R, Vethantham V, Bowman C, Rudnicki M, Dynlacht BD. 2012. Genome-wide identification of enhancers in skeletal muscle: the role of MyoD1. *Gene Dev* **26:** 2763–2779. doi:10.1101/gad.200113.112

Bolger AM, Lohse M, Usadel B. 2014. Trimmomatic: a flexible trimmer for Illumina sequence data. *Bioinformatics* **30:** 2114–2120. doi:10.1093/bioinformatics/btu170

Bricker DK, Taylor EB, Schell JC, Orsak T, Boutron A, Chen Y-C, Cox JE, Cardon CM, Vranken JGV, Dephoure N, et al. 2012. A mitochondrial pyruvate carrier required for pyruvate uptake in yeast, *Drosophila*, and humans. *Science* **337:** 96–100. doi:10.1126/science.1218099

Buenrostro JD, Giresi PG, Zaba LC, Chang HY, Greenleaf WJ. 2013. Transposition of native chromatin for fast and sensitive epigenomic profiling of open chromatin, DNA-binding proteins and nucleosome position. *Nat Methods* **10:** 1213–1218. doi:10.1038/nmeth.2688

Chargé SBP, Rudnicki MA. 2004. Cellular and molecular regulation of muscle regeneration. *Physiol Rev* **84:** 209–238. doi:10.1152/physrev.00019.2003

Chatterjee S, Nam D, Guo B, Kim JM, Winnier GE, Lee J, Berdeaux R, Yechoor VK, Ma K. 2013. Brain and muscle Arnt-like 1 is a key regulator of myogenesis. *J Cell Sci* **126:** 2213–2224.

Chatterjee S, Yin H, Nam D, Li Y, Ma K. 2015. Brain and muscle Arnt-like 1 promotes skeletal muscle regeneration through satellite cell expansion. *Exp Cell Res* **331:** 200–210. doi:10.1016/j.yexcr.2014.08.041

Cirillo F, Resmini G, Ghiroldi A, Piccoli M, Bergante S, Tettamanti G, Anastasia L. 2017. Activation of the hypoxia-inducible factor 1a promotes myogenesis through the noncanonical Wnt pathway, leading to hypertrophic myotubes. *FASEB J* **31:** 2146–2156. doi:10.1096/fj.201600878R

Couteaux R, Mira J, d'Albis A. 1988. Regeneration of muscles after cardiotoxin injury I. Cytological aspects. *Biol Cell* **62:** 171–182. doi:10.1111/j.1768-322X.1988.tb00719.x

DeVilbiss AW, Zhao Z, Martin-Sandoval MS, Ubellacker JM, Tasdogan A, Agathocleous M, Mathews TP, Morrison SJ. 2021. Metabolomic profiling of rare cell populations isolated by flow cytometry from tissues. *Elife* **10:** e61980. doi:10.7554/eLife.61980

Dobin A, Davis CA, Schlesinger F, Drenkow J, Zaleski C, Jha S, Batut P, Chaisson M, Gingeras TR. 2013. STAR: ultrafast universal RNA-seq aligner. *Bioinformatics* **29:** 15–21. doi:10.1093/bioinformatics/bts635

Drouin G, Couture V, Lauzon M-A, Balg F, Faucheux N, Grenier G. 2019. Muscle injury-induced hypoxia alters the proliferation and differentiation potentials of muscle resident stromal cells. *Skelet Muscle* **9:** 18. doi:10.1186/s13395-019-0202-5

Dyar KA, Ciciliot S, Wright LE, Biensø RS, Tagliazucchi GM, Patel VR, Forcato M, Paz MIP, Gudiksen A, Solagna F, et al. 2014. Muscle insulin sensitivity and glucose metabolism are controlled by the intrinsic muscle clock. *Mol Metab* **3:** 29–41. doi:10.1016/j.molmet.2013.10.005

Eliasson P, Jönsson J. 2010. The hematopoietic stem cell niche: low in oxygen but a nice place to be. *J Cell Physiol* **222:** 17–22. doi:10.1002/jcp.21908

Ezashi T, Das P, Roberts RM. 2005. Low O2 tensions and the prevention of differentiation of hES cells. *Proc Natl Acad Sci* **102:** 4783–4788. doi:10.1073/pnas.0501283102

Forcina L, Cosentino M, Musarò A. 2020. Mechanisms regulating muscle regeneration: insights into the interrelated and time-dependent phases of tissue healing. *Cells* **9:** 1297. doi:10.3390/cells9051297

Francetic T, May ML, Hamed M, Mach H, Meyers D, Cole PA, Chen J, Li Q. 2012. Regulation of Myf5 early enhancer by histone acetyltransferase P300 during stem cell differentiation. *Mol Biol* **1:** 5019. doi:10.4172/2168-9547.1000103

Frederick DW, Loro E, Liu L, Davila A, Chellappa K, Silverman IM, Quinn WJ, Gosai SJ, Tichy ED, Davis JG, et al. 2016. Loss of NAD homeostasis leads to progressive and reversible degeneration of skeletal muscle. *Cell Metab* **24:** 269–282. doi:10.1016/j.cmet.2016.07.005

García-Prat L, Perdiguero E, Alonso-Martín S, Dell'Orso S, Ravichandran S, Brooks SR, Juan AH, Campanario S, Jiang K, Hong X, et al. 2020. Foxo maintains a genuine muscle stem-cell quiescent state until geriatric age. *Nat Cell Biol* **22:** 1307–1318. doi:10.1038/s41556-020-00593-7

Ge SX, Jung D, Yao R. 2019. ShinyGO: a graphical enrichment tool for animals and plants. *Bioinformatics* **36:** 2628–2629.

Gharaibeh B, Lu A, Tebbets J, Zheng B, Feduska J, Crisan M, Péault B, Cummins J, Huard J. 2008. Isolation of a slowly adhering cell fraction containing stem cells from murine skeletal muscle by the preplate technique. *Nat Protoc* **3:** 1501–1509. doi:10.1038/nprot.2008.142

Hamed M, Khilji S, Chen J, Li Q. 2013. Stepwise acetyltransferase association and histone acetylation at the Myod1 locus during myogenic differentiation. *Sci Rep* **3:** 2390. doi:10.1038/srep02390

Hardy D, Besnard A, Latil M, Jouvion G, Briand D, Thépenier C, Pascal Q, Guguin A, Gayraud-Morel B, Cavaillon J-M, et al. 2016. Comparative study of injury models for studying muscle regeneration in mice. *PLos One* **11:** e0147198. doi:10.1371/journal.pone.0147198

Harfmann BD, Schroder EA, Kachman MT, Hodge BA, Zhang X, Esser KA. 2016. Muscle-specific loss of Bmal1 leads to disrupted tissue glucose metabolism and systemic glucose homeostasis. *Skelet Muscle* **6:** 12. doi:10.1186/s13395-016-0082-x

Heinz S, Benner C, Spann N, Bertolino E, Lin YC, Laslo P, Cheng JX, Murre C, Singh H, Glass CK. 2010. Simple combinations of lineage-determining transcription factors prime cis-regulatory elements required for macrophage and B cell identities. *Mol Cell* **38:** 576–589. doi:10.1016/j.molcel.2010.05.004

Herzig S, Shaw RJ. 2018. AMPK: guardian of metabolism and mitochondrial homeostasis. *Nat Rev Mol Cell Bio* **19:** 121–135. doi:10.1038/nrm.2017.95

Imai S, Armstrong CM, Kaeberlein M, Guarente L. 2000. Transcriptional silencing and longevity protein Sir2 is an NAD-dependent histone deacetylase. *Nature* **403:** 795–800. doi:10.1038/35001622

Jash S, Adhya S. 2015. Effects of transient hypoxia versus prolonged hypoxia on satellite cell proliferation and differentiation in vivo. *Stem Cells Int* **2015:** 1–9. doi:10.1155/2015/961307

Ji L, Liu Y, Yang C, Yue W, Shi S, Bai C, Xi J, Nan X, Pei X. 2009. Self-renewal and pluripotency is maintained in human embryonic stem cells by co-culture with human fetal liver stromal cells expressing hypoxia inducible factor 1α. *J Cell Physiol* **221:** 54–66. doi:10.1002/jcp.21826

Johnson BP, Walisser JA, Liu Y, Shen AL, McDearmon EL, Moran SM, McIntosh BE, Vollrath AL, Schook AC, Takahashi JS, et al. 2014. Hepatocyte circadian clock controls acetaminophen bioactivation through NADPH-cytochrome P450 oxidoreductase. *Proc Natl Acad Sci* **111:** 18757–18762. doi:10.1073/pnas.1421708111

Józsa L, Réffy A, Demel S, Szilágyi I. 1980. Alterations of oxygen and carbon dioxide tensions in crush-injured calf muscles of rat. *Z Exp Chir* **13:** 91–94.

Kang S, Lee D, Theusch BE, Arpey CJ, Brennan TJ. 2013. Wound hypoxia in deep tissue after incision in rats. *Wound Repair Regen* **21:** 730–739.

Katoku-Kikyo N, Paatela E, Houtz DL, Lee B, Munson D, Wang X, Hussein M, Bhatia J, Lim S, Yuan C, et al. 2021. Per1/Per2–Igf2 axis-mediated circadian regulation of myogenic differentiation. *J Cell Biol* **220:** e202101057. doi:10.1083/jcb.202101057

Koike N, Yoo S-H, Huang H-C, Kumar V, Lee C, Kim T-K, Takahashi JS. 2012. Transcriptional architecture and chromatin landscape of the core circadian clock in mammals. *Science* **338:** 349–354. doi:10.1126/science.1226339

Kuleshov MV, Jones MR, Rouillard AD, Fernandez NF, Duan Q, Wang Z, Koplev S, Jenkins SL, Jagodnik KM, Lachmann A, et al. 2016. Enrichr: a comprehensive gene set enrichment analysis web server 2016 update. *Nucleic Acids Res* **44:** W90–W97. doi:10.1093/nar/gkw377

Landry J, Sutton A, Tafrov ST, Heller RC, Stebbins J, Pillus L, Sternglanz R. 2000. The silencing protein SIR2 and its homologs are NAD-dependent protein deacetylases. *Proc Natl Acad Sci* **97:** 5807–5811. doi:10.1073/pnas.110148297

Langmead B, Salzberg SL. 2012. Fast gapped-read alignment with Bowtie 2. *Nat Methods* **9:** 357–359. doi:10.1038/nmeth.1923

Latroche C, Weiss-Gayet M, Muller L, Gitiaux C, Leblanc P, Liot S, Ben-Larbi S, Abou-Khalil R, Verger N, Bardot P, et al. 2017. Coupling between myogenesis and Angiogenesis during skeletal muscle regeneration is stimulated by restorative macrophages. *Stem Cell Rep* **9:** 2018–2033. doi:10.1016/j.stemcr.2017.10.027

Levine DC, Kuo H-Y, Hong H-K, Cedernaes J, Hepler C, Wright AG, Sommars MA, Kobayashi Y, Marcheva B, Gao P, et al. 2021. NADH inhibition of SIRT1 links energy state to transcription during time-restricted feeding. *Nat Metabolism* **3:** 1621–1632. doi:10.1038/s42255-021-00498-1

L'honoré A, Commère P-H, Negroni E, Pallafacchina G, Friguet B, Drouin J, Buckingham M, Montarras D. 2018. The role of Pitx2 and Pitx3 in muscle stem cells gives new insights into P38α MAP kinase and redox regulation of muscle regeneration. *Elife* **7:** e32991. doi:10.7554/eLife.32991

Li B, Dewey CN. 2011. RSEM: accurate transcript quantification from RNA-seq data with or without a reference genome. *BMC Bioinformatics* **12:** 323. doi:10.1186/1471-2105-12-323

Liu L, Cheung TH, Charville GW, Rando TA. 2015. Isolation of skeletal muscle stem cells by fluorescence-activated cell sorting. *Nat Protoc* **10:** 1612–1624. doi:10.1038/nprot.2015.110

Love MI, Huber W, Anders S. 2014. Moderated estimation of fold change and dispersion for RNA-seq data with DESeq2. *Genome Biol* **15:** 550. doi:10.1186/s13059-014-0550-8

Ly CH, Lynch GS, Ryall JG. 2020. A metabolic roadmap for somatic stem cell fate. *Cell Metab* **31:** 1052–1067. doi:10.1016/j.cmet.2020.04.022

Mahdy MAA, Warita K, Hosaka YZ. 2016. Early ultrastructural events of skeletal muscle damage following cardiotoxin-induced injury and glycerol-induced injury. *Micron* **91:** 29–40. doi:10.1016/j.micron.2016.09.009

Majmundar AJ, Lee DSM, Skuli N, Mesquita RC, Kim MN, Yodh AG, Nguyen-McCarty M, Li B, Simon MC. 2015. HIF modulation of Wnt signaling regulates skeletal myogenesis in vivo. *Development* **142:** 2405–2412.

Mason S, Johnson RS. 2007. The role of HIF-1 in hypoxic response in the skeletal muscle. *Adv Exp Med Biol* **618:** 229–244. doi:10.1007/978-0-387-75434-5_18

McCarthy JJ, Andrews JL, McDearmon EL, Campbell KS, Barber BK, Miller BH, Walker JR, Hogenesch JB, Takahashi JS, Esser KA. 2007. Identification of the circadian transcriptome in adult mouse skeletal muscle. *Physiol Genomics* **31:** 86–95. doi:10.1152/physiolgenomics.00066.2007

Moussaieff A, Rouleau M, Kitsberg D, Cohen M, Levy G, Barasch D, Nemirovski A, Shen-Orr S, Laevsky I, Amit M, et al. 2015. Glycolysis-mediated changes in acetyl-CoA and histone acetylation control the early differentiation of embryonic stem cells. *Cell Metab* **21:** 392–402. doi:10.1016/j.cmet.2015.02.002

Murphy MM, Lawson JA, Mathew SJ, Hutcheson DA, Kardon G. 2011. Satellite cells, connective tissue fibroblasts and their interactions are crucial for muscle regeneration. *Development* **138:** 3625–3637. doi:10.1242/dev.064162

Pal R, Bajaj L, Sharma J, Palmieri M, Ronza AD, Lotfi P, Chaudhury A, Neilson J, Sardiello M, Rodney GG. 2016. NADPH oxidase promotes parkinsonian phenotypes by impairing autophagic flux in an mTORC1-independent fashion in a cellular model of Parkinson's disease. *Sci Rep* **6:** 22866. doi:10.1038/srep22866

Pala F, Girolamo DD, Mella S, Yennek S, Chatre L, Ricchetti M, Tajbakhsh S. 2018. Distinct metabolic states govern skeletal muscle stem cell fates during prenatal and postnatal myogenesis. *J Cell Sci* **131:** jcs212977. doi:10.1242/jcs.212977

Peek CB, Affinati AH, Ramsey KM, Kuo H-Y, Yu W, Sena LA, Ilkayeva O, Marcheva B, Kobayashi Y, Omura C, et al. 2013. Circadian clock NAD^+ cycle drives mitochondrial oxidative metabolism in mice. *Science* **342:** 1243417. doi:10.1126/science.1243417

Peek CB, Levine DC, Cedernaes J, Taguchi A, Kobayashi Y, Tsai SJ, Bonar NA, McNulty MR, Ramsey KM, Bass J. 2017. Circadian clock interaction with HIF1α mediates oxygenic metabolism and anaerobic glycolysis in skeletal muscle. *Cell Metab* **25:** 86–92. doi:10.1016/j.cmet.2016.09.010

Perez-Ramirez CA, Christofk HR. 2021. Challenges in studying stem cell metabolism. *Cell Stem Cell* **28:** 409–423. doi:10.1016/j.stem.2021.02.016

Pettersen IKN, Tusubira D, Ashrafi H, Dyrstad SE, Hansen L, Liu X-Z, Nilsson LIH, Løvsletten NG, Berge K, Wergedahl H, et al. 2019. Upregulated PDK4 expression is a sensitive marker of increased fatty acid oxidation. *Mitochondrion* **49:** 97–110. doi:10.1016/j.mito.2019.07.009

Relaix F, Bencze M, Borok MJ, Vartanian AD, Gattazzo F, Mademtzoglou D, Perez-Diaz S, Prola A, Reyes-Fernandez PC, Rotini A, et al. 2021. Perspectives on skeletal muscle stem cells. *Nat Commun* **12:** 692. doi:10.1038/s41467-020-20760-6

Reske JJ, Wilson MR, Chandler RL. 2020. ATAC-seq normalization method can significantly affect differential accessibility analysis and interpretation. *Epigenet Chromatin* **13:** 22. doi:10.1186/s13072-020-00342-y

Ryall JG, Dell'Orso S, Derfoul A, Juan A, Zare H, Feng X, Clermont D, Koulnis M, Gutierrez-Cruz G, Fulco M, et al. 2015. The NAD^+-dependent SIRT1 deacetylase translates a metabolic switch into regulatory epigenetics in skeletal muscle stem cells. *Cell Stem Cell* **16:** 171–183. doi:10.1016/j.stem.2014.12.004

Sakagami H, Makino Y, Mizumoto K, Isoe T, Takeda Y, Watanabe J, Fujita Y, Takiyama Y, Abiko A, Haneda M. 2014. Loss of HIF-1α impairs GLUT4 translocation and glucose uptake by the skeletal muscle cells. *Am J Physiol Endocrinol Metab* **306:** E1065–E1076.

Scheerer N, Dehne N, Stockmann C, Swoboda S, Baba HA, Neugebauer A, Johnson RS, Fandrey J. 2013. Myeloid hypoxia-

inducible factor-1α is essential for skeletal muscle regeneration in mice. *J Immunol* **191:** 407–414. doi:10.4049/jimmunol.1103779

Scicchitano BM, Sica G, Musarò A. 2016. Stem cells and tissue niche: two faces of the same coin of muscle regeneration. *Eur J Tran Myo* **26:** 6125. doi:10.4081/ejtm.2016.6125

Sebastián D, Guitart M, García-Martínez C, Mauvezin C, Orellana-Gavaldà JM, Serra D, Gómez-Foix AM, Hegardt FG, Asins G. 2009. Novel role of FATP1 in mitochondrial fatty acid oxidation in skeletal muscle cells. *J Lipid Res* **50:** 1789–1799. doi:10.1194/jlr.M800535-JLR200

Shang N, Lee JTY, Huang T, Wang C, Lee TL, Mok SC, Zhao H, Chan WY. 2020. Disabled-2: a positive regulator of the early differentiation of myoblasts. *Cell Tissue Res* **381:** 493–508. doi:10.1007/s00441-020-03237-2

Solanas G, Peixoto FO, Perdiguero E, Jardí M, Ruiz-Bonilla V, Datta D, Symeonidi A, Castellanos A, Welz P-S, Caballero JM, et al. 2017. Aged stem cells reprogram their daily rhythmic functions to adapt to stress. *Cell* **170:** 678–692.e20. doi:10.1016/j.cell.2017.07.035

Soneson C, Love MI, Robinson MD. 2016. Differential analyses for RNA-seq: transcript-level estimates improve gene-level inferences. *F1000Res* **4:** 1521. doi:10.12688/f1000research.7563.2

Stanton MJ, Dutta S, Zhang H, Polavaram NS, Leontovich AA, Hönscheid P, Sinicrope FA, Tindall DJ, Muders MH, Datta K. 2013. Autophagy control by the VEGF-C/NRP-2 axis in cancer and its implication for treatment resistance. *Cancer Res* **73:** 160–171. doi:10.1158/0008-5472.CAN-11-3635

Subramanian A, Tamayo P, Mootha VK, Mukherjee S, Ebert BL, Gillette MA, Paulovich A, Pomeroy SL, Golub TR, Lander ES, et al. 2005. Gene set enrichment analysis: a knowledge-based approach for interpreting genome-wide expression profiles. *Proc Natl Acad Sci* **102:** 15545–15550. doi:10.1073/pnas.0506580102

Sullivan LB, Gui DY, Hosios AM, Bush LN, Freinkman E, Vander Heiden MG. 2015. Supporting aspartate biosynthesis is an essential function of respiration in proliferating cells. *Cell* **162:** 552–563. doi:10.1016/j.cell.2015.07.017

Takahashi JS. 2015. Molecular components of the circadian clock in mammals. *Diabetes Obes Metabolism* **17:** 6–11. doi:10.1111/dom.12514

Tang AH, Rando TA. 2014. Induction of autophagy supports the bioenergetic demands of quiescent muscle stem cell activation. *EMBO J* **33:** 2782–2797. doi:10.15252/embj.201488278

Tanno M, Sakamoto J, Miura T, Shimamoto K, Horio Y. 2007. Nucleocytoplasmic shuttling of the NAD+-dependent histone deacetylase SIRT1*. *J Biol Chem* **282:** 6823–6832. doi:10.1074/jbc.M609554200

Titov DV, Cracan V, Goodman RP, Peng J, Grabarek Z, Mootha VK. 2016. Complementation of mitochondrial electron transport chain by manipulation of the NAD^+/NADH ratio. *Science* **352:** 231–235. doi:10.1126/science.aad4017

Urbani L, Piccoli M, Franzin C, Pozzobon M, Coppi PD. 2012. Hypoxia increases mouse satellite cell clone proliferation maintaining both in vitro and in vivo heterogeneity and myogenic potential. *PLoS One* **7:** e49860. doi:10.1371/journal.pone.0049860

Vaquero A, Scher M, Erdjument-Bromage H, Tempst P, Serrano L, Reinberg D. 2007. SIRT1 regulates the histone methyl-transferase SUV39H1 during heterochromatin formation. *Nature* **450:** 440–444. doi:10.1038/nature06268

Vaughan ME, Wallace M, Handzlik MK, Chan AB, Metallo CM, Lamia KA. 2020. Cryptochromes suppress HIF1α in muscles. *iscience* **23:** 101338. doi:10.1016/j.isci.2020.101338

Wang Z, Zang C, Rosenfeld JA, Schones DE, Barski A, Cuddapah S, Cui K, Roh T-Y, Peng W, Zhang MQ, et al. 2008. Combinatorial patterns of histone acetylations and methylations in the human genome. *Nat Genet* **40:** 897–903. doi:10.1038/ng.154

Wu Y, Tang D, Liu N, Xiong W, Huang H, Li Y, Ma Z, Zhao H, Chen P, Qi X, et al. 2017. Reciprocal regulation between the circadian clock and hypoxia signaling at the genome level in mammals. *Cell Metab* **25:** 73–85. doi:10.1016/j.cmet.2016.09.009

Yang Z, Levison SW. 2006. Hypoxia/ischemia expands the regenerative capacity of progenitors in the perinatal subventricular zone. *Neuroscience* **139:** 555–564. doi:10.1016/j.neuroscience.2005.12.059

Yang X, Yang S, Wang C, Kuang S. 2017. The hypoxia-inducible factors HIF1α and HIF2α are dispensable for embryonic muscle development but essential for postnatal muscle regeneration. *J Biol Chem* **292:** 5981–5991. doi:10.1074/jbc.M116.756312

Yin H, Price F, Rudnicki MA. 2013. Satellite cells and the muscle stem cell niche. *Physiol Rev* **93:** 23–67. doi:10.1152/physrev.00043.2011

Yu G, Wang L-G, He Q-Y. 2015. ChIPseeker: an R/bioconductor package for ChIP peak annotation, comparison and visualization. *Bioinformatics* **31:** 2382–2383. doi:10.1093/bioinformatics/btv145

Yucel N, Wang YX, Mai T, Porpiglia E, Lund PJ, Markov G, Garcia BA, Bendall SC, Angelo M, Blau HM. 2019. Glucose metabolism drives histone acetylation landscape transitions that dictate muscle stem cell function. *Cell Rep* **27:** 3939–3955.e6. doi:10.1016/j.celrep.2019.05.092

Zhang T, Kraus WL. 2010. SIRT1-dependent regulation of chromatin and transcription: linking NAD^+ metabolism and signaling to the control of cellular functions. *Biochim Biophys Act* **1804:** 1666–1675. doi:10.1016/j.bbapap.2009.10.022

Zhang X, Patel SP, McCarthy JJ, Rabchevsky AG, Goldhamer DJ, Esser KA. 2012. A non-canonical E-box within the MyoD core enhancer is necessary for circadian expression in skeletal muscle. *Nucleic Acids Res* **40:** 3419–3430. doi:10.1093/nar/gkr1297

Zhang H, Ryu D, Wu Y, Gariani K, Wang X, Luan P, D'Amico D, Ropelle ER, Lutolf MP, Aebersold R, et al. 2016. NAD^+ repletion improves mitochondrial and stem cell function and enhances life span in mice. *Science* **352:** 1436–1443. doi:10.1126/science.aaf2693

Zhang Y, Masters L, Wang Y, Wu L, Pei Y, Guo B, Parissenti A, Lees SJ, Wang R, Yang G. 2021. Cystathionine γ-lyase/H2S signaling facilitates myogenesis under aging and injury condition. *FASEB J* **35:** e21511.

Zhu P, Zhang C, Gao Y, Wu F, Zhou Y, Wu W-S. 2019. The transcription factor slug represses p16Ink4a and regulates murine muscle stem cell aging. *Nat Commun* **10:** 2568.